Title

New insights into Mn2+ and Mg2+ inhibition of calcite growth

Authors

Mills, Jennifer V
Barnhart, Holly A
DePaolo, Donald J
et al.

Publication Date

2022-10-01

DOI

10.1016/j.gca.2022.06.015

Available online at www.sciencedirect.com

ScienceDirect

Geochimica et Cosmochimica Acta 334 (2022) 338–367

Geochimica et Cosmochimica Acta

www.elsevier.com/locate/gca

New insights into Mn^{2+} and Mg^{2+} inhibition of calcite growth

Jennifer V. Mills [a], Holly A. Barnhart [b], Donald J. DePaolo [c,d], Laura N. Lammers [a,d,*]

[a] Department of Environmental Science, Policy, and Management, University of California-Berkeley, Berkeley, CA 94720, United States
[b] Division of Geological and Planetary Sciences, Caltech, Pasadena, CA 91125, United States
[c] Department of Earth and Planetary Science, University of California-Berkeley, Berkeley, CA 94720, United States
[d] Energy Geosciences Division, Lawrence Berkeley National Laboratory, Berkeley, CA 94720, United States

Received 21 October 2021; accepted in revised form 9 June 2022; Available online 20 June 2022

Abstract

Impurity ion and isotope partitioning into carbonate minerals provide a window into the molecular processes occurring at the fluid-mineral interface during crystal growth. Here, we employ calcium isotope fractionation together with process-based modeling to elucidate the mechanisms by which two divalent cations with starkly contrasting compatibility, magnesium and manganese, inhibit calcite growth and incorporate into the mineral lattice. Calcite growth inhibition by Mg^{2+} is log-linear and K_{Mg} is on the order of 0.02–0.03 throughout the range of $\{Mg^{2+}\}/\{Ca^{2+}\}$ studied here (0.01–2.6). Mn^{2+} exhibits much stronger log-linear growth rate inhibition at low Mn^{2+} concentrations (fluid $\{Mn^{2+}\}/\{Ca^{2+}\} = 0.001–0.02$). Mn^{2+} is readily incorporated into the calcite lattice to form a calcite-rhodochrosite solid solution, with large partition coefficients (K_{Mn} 4.6–15.6) inversely correlated to growth rate. For both Mn^{2+} and Mg^{2+}, calcium isotope fractionation is found to be invariant with $\{Me^{2+}\}/\{Ca^{2+}\}$ despite more than an order of magnitude decline in growth rate. This invariant $\Delta^{44/40}Ca$ suggests that the presence of Mn^{2+} or Mg^{2+} does not significantly change the relative rates of Ca^{2+} attachment and detachment at kink sites during growth, indicative of a dominantly kink blocking inhibition mechanism. Because the partitioning behavior dictates that Mn^{2+} must attach to the surface significantly faster than Ca^{2+}, attachment of Mn^{2+} is likely to be as a non-monomer species such as an ion pair or possibly a larger polynuclear cluster. We propose that calcite growth rate inhibition by Mn is determined by the kinetics of carbonate attachment at Mn-occupied kink sites, potentially due to slow re-orientation kinetics of carbonate ions that have formed an inner-sphere complex with Mn^{2+} at the surface but must reorient to incorporate into the lattice. We demonstrate that patterns in Mg^{2+} partitioning and inhibition behavior are broadly consistent with growth inhibition driven by slow Mg^{2+}-aquo complex dehydration relative to Ca^{2+} but argue that this mechanism likely represents one endmember scenario, seen in Mg-calcite growth at low supersaturations and net precipitation rates. During growth at faster net precipitation rates, some portion of Mg^{2+} is likely incorporated as a partially hydrated or otherwise complexed species, but calcite growth remains significantly inhibited by the kinetics of CO_3^{2-} attachment at Mg^{2+} kink sites. These findings suggest a hybrid classical/nonclassical growth mechanism whereby Ca^{2+} incorporates largely as a free ion at kink sites while Mn^{2+} and some portion of Mg^{2+} are incorporated via non-monomer attachment. This pattern may be generalizable; trace constituent cations with aquo-complex desolvation rates significantly slower than the mineral growth rate preferentially incorporate as a non-monomer species during otherwise classical crystal growth.

Keywords: Magnesium; Manganese; Calcite; Calcium isotope fractionation; Kinetic isotope effect; Trace element partitioning; Nonclassical growth

* Corresponding author at: Department of Environmental Science, Policy, and Management, University of California-Berkeley, Berkeley, CA 94720, United States.

E-mail addresses: jennifer.mills@berkeley.edu (J.V. Mills), hbarnhart@caltech.edu (H.A. Barnhart), djdepaolo@lbl.gov (D.J. DePaolo), lnlammers@berkeley.edu (L.N. Lammers).

https://doi.org/10.1016/j.gca.2022.06.015
0016-7037/

1. INTRODUCTION

Mineral precipitation/dissolution reactions underpin a wide array of geochemical processes relevant to our understanding of both natural and engineered systems, from weathering rates and the long-term carbon cycle (Kump et al., 2000), to water quality and contaminant remediation (Prieto et al., 2013). Yet predicting reaction rates in natural systems remains frustratingly elusive given our limited knowledge of how the micro-scale chemical interactions that occur at mineral-fluid interfaces control the macro-scale kinetics of mineral dissolution and precipitation (Anbeek, 1993; Maher et al., 2006; Maher et al., 2016). Understanding the growth kinetics and trace constituent partitioning behavior of carbonates is of particular interest given their fundamental importance to the paleo-proxy record (Ravizza and Zachos, 2003; Fairchild and Baker, 2012) and key role in climate change mitigation strategies such as geologic carbon storage (Bourg et al., 2015). In particular, various forms of mineral carbonation, including in-situ mineralization of basalts or peridotites (Kelemen et al., 2011; Clark et al., 2020), ambient surficial weathering (Renforth et al., 2009; Beerling et al., 2020; McQueen et al., 2020), and engineered ex-situ mineralization of alkaline waste materials (Gerdemann et al., 2007), are increasingly attractive options for permanent storage of CO_2 (Kelemen et al., 2020). Carbonate solid-solution formation is also a principal remediation technique for contaminants capable of being incorporated into the carbonate lattice (e.g. ^{90}Sr - Lukashev, 1993; Achal et al., 2012).

Geochemists have long sought to develop predictive models for the rate and composition of carbonate minerals growing from complex aqueous solutions typical of natural seawater, pore fluids, cave drip waters, wastewater, and other natural and engineered fluids. Historically, studies of carbonate growth kinetics have focused on the development of empirical rate laws, generally calibrated with bulk precipitation experiments (c.f. Morse et al., 2007). These rate laws form the basis of nearly all reactive transport modeling, but they are most useful for describing reaction kinetics within the narrow range of solution conditions measured. Extending the range of applicability and accurately modeling kinetics, stable isotope fractionation, and trace element partitioning together require an explicit accounting of surface and aqueous composition and speciation (Watkins et al., 2013; Mills et al., 2021). This effort is further complicated by the increasing recognition of non-classical growth mechanisms in systems long thought to fall squarely in the domain of classical crystal growth, including calcium carbonates (Gebauer et al., 2008; Rodriguez-Navarro et al., 2015; Zhu et al., 2016).

To address this critical need, process-based models have been developed that describe carbonate growth kinetics in terms of the elementary reactions of ion addition to and removal from the growing crystal surface (Nielsen et al., 2012; Wolthers et al., 2012; Nielsen et al., 2013). Calcium isotope fractionation during calcite precipitation can be understood and mechanistically modeled in terms of the fluxes of monomer Ca^{2+} ions onto and off of kink sites on the growing crystal surface (Nielsen et al., 2012; Mills et al., 2021). During surface reaction controlled, classical crystal growth, $\Delta^{44/40}Ca$ is dictated by the amount of Ca^{2+} exchange at kink sites on the growing crystal surface (DePaolo, 2011). Calcium isotope discrimination thus provides a window into calcium surface dynamics during calcite growth and represents a new tool for interrogating the complicated suite of processes occurring at the fluid-mineral interface. Here, we put this tool to work to help elucidate calcite growth dynamics in more complex solutions, investigating calcite growth in the presence of manganese and magnesium as representative case studies of impurity ion interaction with the growing mineral.

The presence of non-stoichiometric ions or molecules in solution can influence crystal growth through a number of different mechanisms (De Yoreo and Vekilov, 2003). In *step pinning,* largely irreversible impurity adsorption to a step edge 'pins' the step, meaning that step advancement can only continue by growing around the impurity (Cabrera and Vermilyea, 1958). For a given impurity concentration, this predicts a thermodynamic 'dead zone', or supersaturation below which growth ceases. This occurs when the step curvature must exceed a critical radius to pass between the impurities, and the step becomes undersaturated due to the curvature dependence of the Gibbs-Thomson equation. In *kink blocking*, adsorption of impurity ions at kink sites alters the rate of kink propagation, for example temporarily blocking the propagation of a kink due to slow desolvation kinetics. Foreign ion *incorporation* can also alter growth rates by modifying the stability of the mineral lattice and thus effective supersaturation.

Considering how the presence of foreign ions or molecules in solution can influence calcite growth, impurities can thus be categorized first based on whether or not they are incorporating (capable of partitioning into the lattice). Large organic molecules such as peptides or proteins cannot be readily incorporated into the calcite lattice except as inclusions, and their impact on growth can thus be described as a fully surface-controlled phenomenon (Elhadj et al., 2006; Nielsen et al., 2013). Incorporating ions, on the other hand, can replace a stoichiometric growth unit in the lattice, so the influence of this partitioning on lattice stability must be accounted for.

Incorporating impurities can be further differentiated based on two characteristics: 1) compatibility and 2) preferential partitioning into certain step geometries (Fig. 1). Compatible elements are concentrated in the calcite lattice, with partition coefficients greater than 1, while incompatible elements are depleted in the calcite lattice relative to the fluid, leading to partition coefficients less than 1. Similarly, the $(10\bar{1}4)$ calcite surface displays two non-equivalent step structures, termed acute and obtuse based on the angle formed with the terrace below (Fig. 1A). In addition to well-documented differences in step advancement kinetics (e.g. Teng et al., 2000; Ruiz-Agudo et al., 2010; Stack and Grantham, 2010) and water exchange dynamics (Lardge et al., 2010; Wolthers et al., 2013; De La Pierre et al., 2016), a number of trace elements have been shown to preferentially interact with and incorporate into either the acute or obtuse calcite step (Paquette and Reeder, 1995; Reeder, 1996; Temmam et al., 2000; Wasylenki et al., 2005b). This

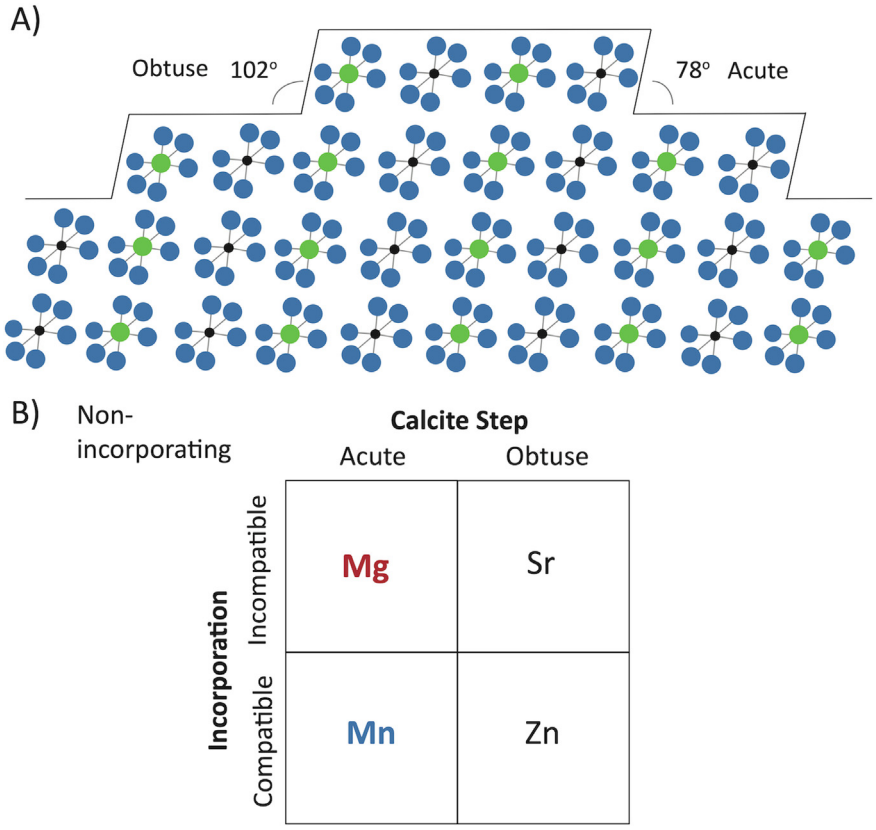

Fig. 1. Diagram synthesizing why Mn^{2+} and Mg^{2+} represent an interesting case-study of how the presence of foreign ions can influence calcite growth. A) The (10 1 4) calcite face displays two non-equivalent step geometries, termed acute and obtuse based on the angle formed with the terrace below. B) Impurities can be categorized first on the basis of whether they are incorporating (capable of partitioning into the lattice) or not; incorporating impurities can be further differentiated on the basis of two parameters: 1) compatibility and 2) preferential partitioning into the acute or obtuse calcite step.

preferential partitioning, termed intrasectoral zoning by Paquette and Reeder (1990), can often be predicted based on the relative size of the substituting ion. Cations larger than Ca^{2+} (e.g. Sr^{2+}, Ba^{2+}, Paquette and Reeder, 1995; Reeder, 1996) and anions larger than CO_3^{2-} (SO_4^{2-} and SeO_4^{2-}, Staudt et al., 1994) tend to partition preferentially into the more geometrically 'open' obtuse step while cations smaller than Ca^{2+} (e.g. Mg^{2+} and Mn^{2+}, Paquette and Reeder, 1995; Wasylenki et al., 2005b) tend to partition preferentially into the more sterically confined acute step. A notable exception to this trend is Zn^{2+}, which partitions preferentially into the obtuse calcite step despite being considerably smaller than Ca^{2+}, possibly due to its electronic configuration (Reeder, 1996; Temmam et al., 2000). While the original experiments by Reeder and colleagues were free-drift experiments performed in unstirred solutions where growth was potentially diffusion-limited, later in-situ AFM experiments (Wasylenki et al., 2005b) confirmed that Mg^{2+} is preferentially incorporated into acute calcite steps during surface-reaction controlled growth.

Manganese and magnesium thus represent an interesting case-study of impurity interaction with the growing calcite surface. They are similar in many ways: both are cations smaller and more strongly hydrated than Ca^{2+} that partition preferentially into the acute step. The effective ionic radius of 6-coordinate Ca^{2+} is 1.0 Å while those of Mg^{2+} and Mn^{2+} are 0.72 Å and 0.83 Å (high-spin state), respectively (Shannon, 1976). Water exchange frequencies (k_{wex}) among the three divalent cations are consistent with their differences in ionic potential: Helm and Merbach (1999) place the k_{wex} of Mg^{2+} at $6.7e5s^{-1}$ and Mn^{2+} at $2e7s^{-1}$ while the water exchange frequency of Ca^{2+} is greater than $2e8s^{-1}$. But Mg^{2+} and Mn^{2+} exhibit radically different compatibility with the calcite lattice. Mn^{2+} is highly compatible, with strongly rate-dependent partitioning; reported partition coefficients range from <5 to upwards of 30 (Lorens, 1981; Pingitore et al., 1988; Dromgoole and Walter, 1990b; Dromgoole and Walter, 1990a). In contrast, Mg^{2+} is highly incompatible, with partition coefficients in the range of ~0.01–0.035 (Mucci and Morse, 1983; Mucci, 1987; Mavromatis et al., 2013; Gabitov et al., 2014).

As the major inhibitor cation in seawater, Mg^{2+} inhibition of calcite growth and concomitant partitioning behavior has been well-studied, both in seawater and simple electrolyte solutions (Berner, 1975; Mucci and Morse, 1983; Mucci, 1987; Davis et al., 2000b; Wasylenki et al., 2005b; Stephenson et al., 2011; Mavromatis et al., 2013; Gabitov et al., 2014). However, the mechanism by which Mg^{2+} acts to inhibit calcite growth remains contested. Berner (1975) first argued that calcite growth inhibition

by Mg^{2+} was driven by a largely solid solution thermodynamic effect, where Mg^{2+} incorporation yielded magnesian calcites considerably more soluble than pure calcite. Subsequent interpretations of bulk growth data invoked the stronger hydration of Mg^{2+} relative to Ca^{2+} to argue for a kink-blocking mechanism driven by Mg^{2+} adsorption followed by slow dehydration (Reddy and Wang, 1980; Mucci and Morse, 1983). Observations of near-linear declines in step velocity with increasing solution Mg^{2+} from in-situ AFM experiments were then interpreted as indicative of solid solution thermodynamic inhibition (Davis et al., 2000b). A later in-situ AFM study by Astilleros et al. (2010), run at higher solution Mg/Ca, argued against this interpretation on the basis of existing calcite-magnesite solid solution thermodynamic data. Recent interpretations based on microkinetic models of calcite growth similarly argue for dominantly kink-blocking inhibition (Nielsen et al., 2013; Dobberschütz et al., 2018).

The interaction between Mn^{2+} and carbonate minerals is also of considerable geochemical interest; the Mn content of carbonates is often used to infer the redox conditions of the depositional environment (Barnaby and Rimstidt, 1989) and thus as a marker of diagenetic alteration (Brand and Veizer, 1980). While a number of studies have examined Mn^{2+} partitioning into calcite (Lorens, 1981; Mucci, 1988; Pingitore et al., 1988; Dromgoole and Walter, 1990b; Dromgoole and Walter, 1990a), fewer well-controlled kinetic studies have been performed. By far the most extensive dataset was collected by Dromgoole and Walter (Dromgoole and Walter, 1990a; Dromgoole and Walter, 1990b), who investigated Mn^{2+} inhibition of calcite growth and associated partitioning behavior as a function of temperature, P_{CO2}, and $\{Mn^{2+}\}/\{Ca^{2+}\}$ in $CaCl_2$ solutions. They found that Mn^{2+} strongly inhibits calcite growth and that trends in the extent of inhibition with $\{Mn^{2+}\}/\{Ca^{2+}\}$ were roughly consistent with a Langmuir adsorption model (Dromgoole and Walter, 1990a). Notably, Mucci (1988) reported that in seawater solutions, the addition of Mn^{2+} actually increased calcite growth rates, potentially due to competitive adsorption with Mg^{2+} or $MgSO_4$ complexes (Nielsen et al., 2016). While these observations could point towards a dominantly kink blocking inhibition mechanism, the extent to which changes in lattice solubility with considerable Mn^{2+} incorporation influence growth kinetics remains largely unconstrained. Predicting partitioning behavior based on mechanistic principles, particularly for highly compatible elements, also remains a key challenge. Previous studies have documented a strong kinetic control on Mn^{2+} partitioning into calcite (Dromgoole and Walter, 1990b; Lorens, 1981), the implications of which will be explored here.

Mills et al. (2021) introduced the concept that calcium isotope fractionation could differentiate between these different mechanisms of growth inhibition. In brief, destabilization of the mineral lattice due to impurity incorporation should increase the flux of Ca off the surface at a given $\{Ca^{2+}\}$ and $\{CO_3^{2-}\}$ and thus decrease the magnitude of $\Delta^{44/40}Ca_{calcite\text{-}fluid}$. In contrast, $\Delta^{44/40}Ca$ is predicted to be invariant with impurity concentration for dominantly kink blocking inhibition, as inhibitor adsorption to kink sites and resultant modification of kink propagation kinetics will not change the *relative* rate of Ca attachment to vs. removal from the surface.

Here, we attempt to operationalize the use of stable isotopes as molecular probes of crystal growth, employing calcium isotope fractionation to help elucidate the mechanism by which two divalent cations with starkly contrasting compatibility, magnesium and manganese, interact with the growing calcite surface and inhibit growth. We present results from a series of constant-composition (chemostat) inorganic calcite growth experiments where all aspects of solution chemistry are held constant while $\{Mn^{2+}\}/\{Ca^{2+}\}$ is varied. Observed trends in rate inhibition, trace element partitioning, and isotope fractionation are interpreted using an ion-by-ion kinetic framework to develop a molecular-level understanding of Mn^{2+} and Mg^{2+} inhibition of calcite growth.

2. METHODS

A series of constant composition calcite growth experiments were performed to investigate the interplay between Mn and Mg inhibition of calcite growth, partitioning into the lattice, and Ca isotope fractionation. Independent seeded Mn-calcite and Mg-calcite growth experiments were run under different fluid metal to calcium (Me/Ca) ratios ($\{Mn^{2+}\}/\{Ca^{2+}\}$ = 0.002 – 0.124; $\{\{Mg^{2+}\}/\{Ca^{2+}\}$ = 0.01 – 2.6).

2.1. Constant composition calcite growth experiments

2.1.1. Experimental setup

Constant composition calcite growth experiments with varied Me/Ca ratios were performed using the chemostat reactor setup and methodology described in Mills et al. (2021). In brief, an automated titration system controlled by solution pH measurement is used to maintain constant solution conditions in a 2L pyrex growth chamber containing 1.8L of growth solution (Fig. S1). As calcite precipitates over the course of an experiment, the decrease in solution pH triggers the addition of equimolar (Me,Ca) Cl_2 and K_2CO_3 titrant solutions (0.25 M) to return the pH to the set point (8.0), thus replacing the growth units removed from solution through precipitation. The ratio of Mn/Ca or Mg/Ca in the 0.25 M cation titrant solution is dictated by the Me/Ca distribution coefficient, which complicates the design of constant composition growth experiments for highly compatible elements, as discussed below.

2.1.2. Materials and solution preparation

Two suites of seeded growth experiments were completed (Table 1) in which all aspects of solution chemistry were held constant except for the concentration of Mn or Mg in the growth solution. All experiments were run at a fixed solution pH (8.0 ± 0.1), ionic strength (0.1 M, adjusted with KCl), temperature (25 ± 0.5 °C), and calcite saturation (SI = 0.8), where:

Table 1
Summary of experimental solution conditions.

Exp.	Calcite seed			Steady-state concentration			Steady-state activity				$SI_{calcite}$	Titrant
		$[Ca]_b$	$[Ca]_{end}$	[Ca]	[Me]	Alkalinity	$\{Ca^{2+}\}$	$\{Me^{2+}\}$	$\{Me^{2+}\}/\{Ca^{2+}\}$	$\{Ca^{2+}\}/\{CO_3^{2-}\}$		[Me]/[Ca]
units	g	mM	mM	mM	mM	meq/L	mM	mM	–	–	–	–
Mn2	0.504	3.86	3.82	3.81	0.023	4.03	1.47	0.0072	0.0049	112.1	0.81	0.027
Mn3	0.502	3.86	3.53	3.63	0.039	4.06	1.40	0.012	0.0087	105.9	0.79	0.060
Mn5	1.001	3.85	3.70	3.73	0.201	4.02	1.42	0.062	0.044	109.9	0.79	0.67
Mn6	1.004	3.86	3.63	3.75	0.478	4.20	1.41	0.146	0.104	105.8	0.80	1.51
Mn7	1.001	3.84	3.67	3.76	0.097	4.08	1.43	0.030	0.021	108.8	0.80	0.23
Mn8	0.501	3.83	3.63	3.74	0.023	4.01	1.43	0.0072	0.0050	109.8	0.80	0.028
Mn9	0.500	3.82	3.62	3.66	0.0068	4.03	1.40	0.0022	0.0016	106.9	0.79	0.0074
Mn11	0.500	3.78	3.50	3.66	0	4.03	1.40	0	0	106.7	0.79	0
Mn12	0.502	3.79	3.60	3.68	0.008	4.05	1.40	0.0025	0.0018	106.9	0.79	0.0080
Mn13	1.001	3.77	3.69	3.72	0.567	4.23	1.39	0.172	0.124	104.1	0.80	1.73
Mg2	1.005	3.77	3.58	3.70	0.42	4.07	1.42	0.18	0.124	107.5	0.80	0.003
Mg3	1.001	3.79	3.62	3.70	4.22	4.10	1.43	1.78	1.243	110.1	0.80	0.026
Mg4	0.501	3.80	3.57	3.67	0.042	4.03	1.42	0.018	0.012	108.3	0.80	0.0004
Mg5	1.006	3.81	3.73	3.77	2.09	4.14	1.46	0.88	0.604	109.9	0.82	0.013
Mg7	1.007	3.82	3.63	3.75	8.90	4.31	1.47	3.81	2.589	110.1	0.82	0.064

$$SI = log_{10}\left(\frac{\{Ca^{2+}\}\{CO_3^{2-}\}}{K_{sp}}\right) \quad (2.1)$$

Solution speciation and calcite saturation were determined using PHREEQC (Parkhurst and Appelo, 2013), with the llnl.dat thermodynamic database and calcite equilibrium constant $K_{sp} = 10^{-8.48}$ (Plummer and Busenberg, 1982). Supersaturations are reported as calculated by PHREEQC based on the analytic expressions for the temperature dependence of calcite solubility. Measured values for Mn-(bi)carbonate ion pair stability constants as well as the K_{sp} for rhodochrosite span 2 orders of magnitude and this measurement spread is reflected in the geochemical thermodynamic databases (Fig. S2). The choice of thermodynamic database thus has a non-negligible impact on calculated Mn speciation for the experimental solutions considered here. The llnl.dat database was used for speciation calculations throughout this study as it assumes a 'middle ground' rhodochrosite solubility ($K_{sp} = 10^{-10.5}$; Morgan, 1967; Johnson, 1982; Robie et al., 1984) representative of the center of the normal distribution of reported values (Fig. S2A) as well as ion pair stability constants consistent with existing measurements (Fig. S2B,C).

The experiments were seeded using either 0.5 g or 1 g of Baker-analyzed calcite as seed material, used directly as obtained from the manufacturer with no pre-treatment. The larger amount of seed was used in the higher Mn or Mg, slower-growing experiments to minimize the influence of pH drift and heterogeneous nucleation on the pH probe, which can become problematic in longer experiments (>1 day). Solutions were prepared by dissolving ACS reagent grade chemicals (Sigma-Aldrich) in ultrapure water (18.22MΩ, Milli-Q). All Ca solutions were prepared using the same 1.8 M $CaCl_2{\cdot}2H_2O$ stock solution. A 1 or 0.1 M $MgCl_2{\cdot}6H_2O$ stock solution was used to prepare Mg solutions; a new 1 M $MgCl_2{\cdot}6H_2O$ solution was prepared before experiment Mg7 (Table 1). To prevent Mn^{2+} oxidation, all solutions were prepared with N_2-sparged water and fresh $MnCl_2{\cdot}4H_2O$ stock solutions were prepared just before every experiment. A solution pH of 8.0 was also chosen as a trade-off between slower Mn oxidation kinetics at low pH (Hem, 1963; Morgan, 2005) and maintaining a relatively low Ca^{2+}:CO_3^{2-} activity ratio (Ca^{2+}:CO_3^{2-} = 100; previous studies of Mn calcite growth inhibition used notably high Ca^{2+}:CO_3^{2-} (Lorens, 1981; Mucci, 1988; Dromgoole and Walter, 1990b; Dromgoole and Walter, 1990a).

Titrant solutions (0.25 M (Me,Ca)Cl_2, 0.25 M K_2CO_3) were prepared at the start of each experiment and stored in gas-tight Tedlar bags (Sigma-Aldrich). The appropriate Me/Ca for the cation titrant solution is dictated by the trace constituent's distribution coefficient: To maintain constant solution conditions, the titrant Me/Ca should match the Me/Ca of the solid phase being precipitated. For highly incompatible elements such as Mg, a rough estimate of the partition coefficient (here, $K_{Mg} \sim 0.02$ was assumed (Mucci and Morse, 1983; Mavromatis et al., 2013)) is adequate. So little Mg is removed from solution relative to the size of the growth solution Mg reservoir that even substantial deviations from the assumed K_d will not substantially

change solution Mg concentrations. For highly compatible elements such as Mn, it is much more difficult to maintain constant solution conditions. Slight offsets between the titrant concentration and solid Mn/Ca dictated by the partition coefficient can lead to large changes in the growth solution Mn concentration given the small size of the growth solution Mn reservoir relative to that in the titrant. As discussed below, this is advantageous in that changes in growth solution [Mn] can be used to constrain the Mn partition coefficient. However, the large partition coefficients also present an experimental challenge: one must either know the partition coefficient for a given set of solution conditions a-priori or determine the K_d through trial and error in successive experiments.

Initial testing revealed that as long as the titrant concentration is relatively close to that dictated by the K_{Mn}, solution Mn concentrations evolves to a steady-state over the course of an experiment (Fig. S3). Most practically, this allowed us to run near-constant Mn concentration experiments with minimal trial-and error. In the steady-state region, the titrant Mn/Ca matches that being removed from solution, thus revealing the K_{Mn} for the steady-state solution $\{Mn^{2+}\}/\{Ca^{2+}\}$. A single replicate experiment with initial conditions adjusted to match the steady-state $\{Mn^{2+}\}/\{Ca^{2+}\}$ thus generally yielded solution Mn concentrations that varied <10% over the course of the experiment. This self-stabilizing behavior observed in growth solution [Mn] is the first indication of a strong negative feedback between calcite growth rate and Mn partitioning (Section 4.2.1, Fig. 8). If the titrant concentration over-predicts the partition coefficient, solution Mn concentrations will rise, thus decreasing growth rates. The fact that Mn concentrations stabilize instead of continuing to increase points towards a negative feedback between growth rate and K_d: the declining rates increase the partition coefficient until the Mn being removed through precipitation matches that being added via titration.

2.1.3. Experimental run description

Each experiment was started by combining 0.9L cation ($(Me,Ca)Cl_2$) and anion ($KHCO_3$ + KCl) solutions in the growth chamber and purging the headspace with N_2 before attaching the chamber lid (sealed with an o-ring). The solution pH was adjusted to 8.0 with 0.1 M KOH, the automated titration program was started, and calcite seed was then added through a port in the chamber lid to initiate precipitation. Solution conditions were monitored throughout an experiment by taking 5–20 mL fluid aliquots through the sample port at regular intervals. Samples were passed through 0.2 μm syringe filters to remove any solids; aliquots for cation concentration analysis were immediately acidified by 15 N HNO_3 while aliquots for alkalinity analysis were stored (unacidified) in 15 mL falcon tubes with minimal headspace until analysis (within 1 h of sampling). At the end of an experiment, the solution was vacuum filtered through a 0.45 μm nylon membrane filter to collect the precipitated material, which was rinsed 3x with Milli-Q H_2O and dried at room temperature in a fume hood. Experimental duration was dictated by the titration volume (equivalently moles $(Me,Ca)CO_3$ precipitated) to achieve ~1 turnover of the Ca reservoir. Importantly, for the Mn suite of experiments, this meant longer experiments and higher total titration volumes for high $\{Mn^{2+}\}$ experiments, as the $(Me,Ca)Cl_2$ titrant contained significantly less Ca^{2+} (Table 1).

2.2. Analytical techniques

Changes in growth solution Ca, Mn, and Mg concentration over the course of an experiment and in resultant solids were measured by ICP-OES (Perkin Elmer 5300 DV, uncertainty ~5% based on repeat analysis of standards). Precise Ca concentrations for initial and end fluids samples were obtained from isotope-dilution measurements (uncertainty ~1%) during Ca isotope analysis. Alkalinity was measured by Gran-titration with calibrated 0.01 M H_2SO_4. The surface area of the calcite seed material was measured as the N_2 BET surface area at 77 K (3Flex, Micromeritics). The morphology of the solids precipitated was examined using scanning electron microscopy (SEM, Zeiss EVO-10 Variable Vacuum; samples were carbon-coated prior to analysis and imaged in secondary electron mode). The mineralogy of the $(Me,Ca)CO_3$ precipitates was analyzed using powder X-Ray diffraction. The $(Mg,Ca)CO_3$ samples were analyzed on a PANalytical X-Pert Pro diffractometer equipped with a Co x-ray source; data was collected between 20° and 70° 2θ. The $(Mn,Ca)CO_3$ samples were analyzed on a Rigaku SmartLab diffractometer equipped with a Cu x-ray source; data was collected between 15° and 65° 2θ. Peak fitting and identification was performed with X'Pert HighScore Plus for the $(Mg,Ca)CO_3$ samples and QualX for the $(Mn,Ca)CO_3$ samples. GSAS-II was used for Reitveld refinement. The detection limit for the identification of distinct phases (including aragonite and rhodochrosite) was approximately 2–5% by volume.

Calcium isotope ratios and elemental Ca concentrations were measured using the method described in Mills et al. (2021). Briefly, the calcium isotope composition was measured with a Finnigan TRITON thermal ionization mass spectrometer (TIMS) using the double spike method (^{42}Ca + ^{48}Ca), and calcium separation was performed via column chemistry using Ca-specific DGA resin (Eichrom). All Ca isotope ratios are expressed in standard delta notation relative to bulk silicate earth (BSE - $^{44}Ca/^{40}Ca$ = 0.0212035) as:

$$\delta^{44/40}Ca = \left(\frac{\left(^{44}Ca/^{40}Ca\right)_{sample}}{\left(^{44}Ca/^{40}Ca\right)_{BSE}} - 1\right)1000 \quad (2.2)$$

The NIST SRM 915a reference material was measured 3x per turret and used to determine external analytical uncertainty on $\delta^{44/40}Ca$ measurements. SRM 915a measurements averaged to −0.94‰ with an external 2σ reproducibility of ±0.15‰ (n = 12).

2.3. Growth rate determination

The calcite growth rate in mol/s was determined from the experimental titration rate:

$$R(mol/s) = C * \frac{dV}{dt} \quad (2.3)$$

where C is the titrant concentration (0.25 M) and $\frac{dV}{dt}$ is the slope of the titrant volume versus time curve. To obtain surface-normal growth rates (mol/m^2/s), this rate was normalized by the BET surface area of the seed crystal (specific surface area, SSA = 0.21 ± 0.01 m^2/g). The raw growth rate (mol/s) was calculated for the 5–10 mL titration interval for each experiment, constraining the growth rate calculation to the early stages of the experiment where surface area is best defined (majority of surface area is provided by the seed crystal) but avoiding the first few mL titrated where Mn concentrations had not yet reached steady-state (Section 2.2, Fig. S3). The grams of material precipitated over the 0–7.5 mL titration interval were accounted for in the calculation of surface area. The inter-experiment reproducibility, quantified as the average difference between near-replicates in the Mn suite of experiments, was 6.7%. Propagating this inter-experiment reproducibility with the 5% uncertainty on the BET surface area measurement yields an overall uncertainty of 8.4%. The impact of titration interval used to calculate the growth rate was also considered; calculating the growth rate based on different titration intervals within a single experiment (e.g. 5–10 mL vs. 10–15 mL) yielded an average relative difference of 3% for the Mn experiments and 6% for the Mg experiments. The analytical uncertainty of the surface-normal growth rates measured was thus taken to be the larger of the 8.4% inter-experiment uncertainty and observed intra-experiment variability.

2.4. Partition coefficient calculation

Partition coefficients for manganese (K_{Mn}) and magnesium (K_{Mg}) were calculated as:

$$K_{Me} = \frac{(Me/Ca)_{calcite}}{\left(\{Me^{2+}\}/\{Ca^{2+}\}\right)_{fluid}} \quad (2.4)$$

where $(Me/Ca)_{calcite}$ is the molar ratio of Me to Ca in the overgrowth and $\left(\{Me^{2+}\}/\{Ca^{2+}\}\right)_{fluid}$ is the steady-state growth solution Me^{2+} to Ca^{2+} activity ratio. For comparison to literature datasets where sufficient data to calculate solution activities was not provided, $K_{Me,conc}$ is also presented using the fluid Me/Ca concentration ratio in the denominator.

The total Mn or Mg concentration in the experimental solids was determined by dissolving a weighed aliquot of the dried solid with 2% HNO_3 and measuring Mn, Mg, and Ca elemental concentrations via ICP-OES by the same method used for the experimental solutions (Section 2.2). The Me content of the bulk solid (seed + overgrowth) is almost exclusively derived from the overgrowth. The Baker-analyzed seed material used contained <0.01% Mn and Mg; the Mn content of bulk solids from the Mg experiments was never above instrument background and vice versa. The overgrowth composition was thus calculated as:

$$\left(\frac{Me}{Ca}\right)_{overgrowth} = \frac{\left(\frac{molMe,bulk}{g,bulk}\right)(g,bulk)}{\left(\frac{molCa,bulk}{g,bulk}\right)(g,bulk) - molCa,seed} \quad (2.5)$$

where the moles Mn or Mg per gram of bulk solid $\left(\frac{molMe,bulk}{g,bulk}\right)$ was derived directly from the ICP concentration measurement and the total grams of bulk solid $(g,bulk)$ is the mass of seed material + the mass of overgrowth precipitated $(g,overgrowth)$, calculated as:

$$g,overgrowth = MW_{overgrowth} * [CaCl_{2,titrant} + MeCl_{2,titrant}] * volume\ \ titrated \quad (2.6)$$

where MW is the molecular weight.

For the Mg experiments, so little Mg is incorporated into the lattice that the solid solution molecular weight is approximately equal to that of calcite ($MW_{overgrowth} \sim MW_{calcite} = 100.09$ g/mol), while for the Mn experiments, $MW_{overgrowth}$ is estimated using the titrant Mn composition to generate an approximate mole fraction Mn ($MW_{overgrowth} \sim (X_{Mn} * MW_{rhodochrosite}) + ((1\text{-}X_{Mn}) * MW_{calcite})$). The Mn overgrowth composition calculated in this manner is highly consistent with the changes in lattice parameters observed via powder XRD (Section 3.2). In all experiments, the overgrowth represented 40–60% of the bulk solid by weight.

For the Mn experiments, the partition coefficient can also be calculated directly from the evolution of growth solution Mn. As described in Section 2.2, fluid Mn concentrations were observed to approach a steady-state over the course of the experiment (Fig. S3). In this steady-state region, a roughly equal number of moles of Mn are being added to and removed from solution, meaning that the titrant Mn/Ca matches the composition of the overgrowth. The partition coefficient can thus be calculated from the titrant Mn/Ca and the steady-state fluid activity ratio:

$$K_{Mn,fluid} = \frac{(Mn/Ca)_{titrant}}{\left(\{Mn^{2+}\}/\{Ca^{2+}\}\right)_{fluid}} \quad (2.7)$$

This fluid partition coefficient calculation homes in on the steady-state interval where $\{Mn^{2+}\}/\{Ca^{2+}\}$ is well-constrained - $[Mn^{2+}]$ varies up by 10% transiently before steady-state is achieved. Partition coefficients calculated from the solid and fluid data are compared in Fig. S4. In all cases, K_{Mn} calculated using the two methods is within 5%, except for the highest Mn experiment (Mn 13) where the partition coefficient calculated from the solid composition is 8.5% higher than that calculated from the fluids (Table 2). In subsequent figures, we plot the average of the solid and fluid K_{Mn}.

2.5. Calculation of calcium isotope fractionation

The calcium isotope fractionation factor between the solid and aqueous solution (eq (2.8)) was calculated using a Ca isotope box model as described in Mills et al. (2021), using the evolution of $\delta^{44}Ca_{fluid}$ over the course of an experiment to constrain $\Delta^{44/40}Ca_{calcite\text{-}fluid}$.

$$\Delta^{44/40}Ca_{calcite-fluid} = \delta^{44/40}Ca_{calcite} - \delta^{44/40}Ca_{fluid} \approx 1000\ln(\alpha_p) \quad (2.8)$$

Briefly, the change in growth solution Ca over time is:

$$\frac{dCa_{fluid}}{dt} = F_{in} - F_{out} \quad (2.9)$$

where F_{in} is the flux of Ca into the growth solution (i.e. titration rate - mol/s) and F_{out} is the flux of Ca out of solution via precipitation. The change in $\delta^{44}Ca_{fluid}$ over time can similarly be modeled by tracking ^{40}Ca and ^{44}Ca separately:

$$\frac{d^{44}Ca_{fluid}}{dt} = \frac{R_{in}}{R_{in}+1}F_{in}(t) - \frac{R_{calcite}(t)}{R_{calcite}(t)+1}F_{out}(t) \quad (2.10)$$

$$\frac{d^{40}Ca_{fluid}}{dt} = \frac{1}{R_{in}+1}F_{in}(t) - \frac{1}{R_{calcite}(t)+1}F_{out}(t) \quad (2.11)$$

$$R_{fluid}(t) = \frac{^{44}Ca_{fluid}(t)}{^{40}Ca_{fluid}(t)} \quad (2.12)$$

$$R_{calcite}(t) = \alpha_p R_{fluid}(t) \quad (2.13)$$

where $R_{in,}$ $R_{fluid}(t)$, and $R_{calcite}(t)$ are the 44/40Ca ratio of the $CaCl_2$ titrant solution (constant), growth solution, and precipitated calcite at a given point of time, respectively. Equations (2.10)–(2.13) were solved numerically by finite difference in MATLAB. This allowed any changes in the size of the Ca reservoir due to titrant offset or CO_2 degassing to be accounted for. CO_2 degassing raises the solution pH, which can mask the pH drop due to carbonate precipitation, leading to lower titrant addition than required to replace the Ca^{2+}, CO_3^{2-}, and trace constituents removed from solution. $\Delta^{44/40}Ca_{calcite\text{-}fluid}$ was calculated as the average of the range of α_p that yielded measured $\delta^{44}Ca_{fluid,final}$ within 2σ uncertainty. The analytical uncertainty of calculated $\Delta^{44/40}Ca_{calcite\text{-}fluid}$ was taken to be the larger of the 2σ uncertainty calculated through formal error propagation of a steady-state box model:

$$\Delta^{44/40}Ca_{calcite-fluid} = \frac{\delta^{44/40}Ca_{fluid,initial} - \delta^{44/40}Ca_{fluid,final}}{1 - e^{-(moles\ \ Ca\ \ titrated/moles\ \ Ca\ \ \ growth\ \ \ solution)}} \quad (2.14)$$

and the entire potential range of fractionations yielding measured final $\delta^{44}Ca_{fluid}$.

3. RESULTS

Experimental solution conditions and results are summarized in Tables 1 and 2, respectively.

3.1. Crystal morphology in the presence of Mn and Mg

The Mn^{2+}-bearing growth experiments yielded (Mn,Ca)CO_3 overgrowths with compositions ranging from 0 to 64 mol % $MnCO_3$ (Table 2). SEM images of these precipitates reveal irregular rhombohedra and changes in surface texturing with increasing solution and solid Mn/Ca (Figs. S6, 2). The edges of the Mn-calcite rhombohedra begin to roughen in experiment Mn8 (fluid $\{Mn^{2+}\}/\{Ca^{2+}\} = 0.005$, 3% $MnCO_3$ - Fig. S6D, Fig. 2B). At higher fluid $\{Mn^{2+}\}/\{Ca^{2+}\}$, two features emerge. First, jagged macro-steps appear, leading to an almost jigsaw puzzle effect of rough-edged lobes on the crystal face (Fig. 2C). Then, the surface becomes textured by smaller, rounded domains and occasional, sub-μm elongate particles (Fig. 2D-F). In interpreting these morphological differences, it is also important to recognize that the higher $\{Mn^{2+}\}/\{Ca^{2+}\}$ experiments were run for longer and to higher total titration volumes in order to achieve roughly the same turnover of the Ca reservoir for Ca isotope analysis. Thus more of the sample is composed of (Mn,Ca)CO_3 overgrowth in the higher Mn-content samples, though between 45 and 63% of the sample is overgrowth in all instances (Table 2).

In an in-situ AFM study of calcite growth in the presence of Mn^{2+}, Astilleros et al. (2002) observe similar changes in surface morphology with increasing solution Mn^{2+}. In the lowest Mn^{2+} concentration studied ($\{Mn^{2+}\} = 0.021$, roughly comparable to experiment Mn3 here, with $\{Mn^{2+}\} = 0.012$ and 6% $MnCO_3$), the initially straight calcite step edges become rounded and distorted, developing lobes during growth. At higher Mn ($\{Mn^{2+}\} = 0.096$), Astilleros et al. (2002) report a cessation of step advancement once the original calcite surface was fully coated and a transition to two-dimensional (2D) nucleation-driven growth. In an in-situ scanning force microscopy study of calcite precipitation in the presence of PO_4^{3-}, Dove and Hochella (1993) observe a similar transition from straight to jagged, widely spaced steps in 10 μM PO_4^{3-}, accompanied by the formation of rounded surface nuclei. Observations of morphological changes during calcite growth in the presence of Mg^{2+} have further demonstrated the potential for 'surface segmentation', in which mosaic-like surface texturing occurs through the formation of separate and independently growing crystal segments (Sethmann et al., 2010; Pimentel et al., 2013; Hong et al., 2016). The development of this surface segmentation has been explained in terms of the build up of strain due to the lattice mismatch between pure calcite and the precipitating solid solution (Sethmann et al., 2010; Pimentel et al., 2013; Hong et al., 2016). The surface texturing observed here at fluid $\{Mn^{2+}\}/\{Ca^{2+}\} > 0.02$ could thus be indicative of this strain-induced segmentation.

Comparable surface texturing is not observed in the Mg^{2+} inhibition experiments (Fig. 3) where far less Mg^{2+} was incorporated into the calcite lattice; overgrowth composition ranged from 0 to 7 mol % $MgCO_3$ (Table 2). Instead, the dominant morphological change with increasing fluid $\{Mg^{2+}\}/\{Ca^{2+}\}$ is the development of crystal faces not expressed in {104} rhombohedral calcite (Fig. 3C-F). As commonly observed for calcite grown in the presence of Mg^{2+}, increasing fluid $\{Mg^{2+}\}/\{Ca^{2+}\}$ led to elongated crystal forms with apparent (110) and (100) calcite faces progressively increasingly expressed over the (104) face (Zhang and Dawe, 2000; Davis et al., 2004; Jiménez-López et al., 2004). Initially interpreted to represent selective interaction of Mg^{2+} with certain crystal faces (Folk, 1974; Zhang and Dawe, 2000), Davis et al. (2004) further interpreted the formation of such pseudo-facets in terms of preferential Mg incorporation into acute calcite steps (Paquette and Reeder, 1995; Wasylenki et al., 2005b) and the accumulation of strain at the intersection of non-equivalent step types. In addition, aragonite needles are observed in the highest Mg experiment (Mg7, $\{Mg^{2+}\}/\{Ca^{2+}\} = 2.6$, Fig. 3F). A change in slope of the titration

Table 2
Growth rate inhibition, Ca isotope fractionation ($\Delta^{44/40}Ca_{calcite\text{-}fluid}$), and partitioning results.

Exp.	Growth rate					Distribution Coefficient				Solid Composition			
		error*	$\Delta^{44/40}Ca$	2σ error	f_{OG}^{**}	K_D[a]	error	K_D[b]	error	Mol % $MeCO_3$[a]	error	Mol % $MeCO_3$[b]	error
units	mol/m^2/s		‰										
Mn2	1.64E−06	1.37E−07			0.50	5.6	0.4	6.1	0.5	2.7	0.14	2.9	0.2
Mn3	1.40E−06	1.18E−07	−1.40	0.14	0.60	6.9	0.5	7.3	0.7	5.7	0.29	6.0	0.4
Mn5	1.94E−07	1.63E−08	−1.35	0.13	0.51	15.2	1.2	15.9	1.4	40.0	2.04	41.1	2.9
Mn6	2.53E−07	2.13E−08	−1.41	0.15	0.61	14.6	1.1	15.0	1.3	60.2	3.07	60.8	4.3
Mn7	4.25E−07	3.57E−08	−1.32	0.1	0.45	11.2	0.9	10.8	1.0	19.0	0.97	18.4	1.3
Mn8	2.01E−06	1.69E−07	−1.44	0.11	0.60	5.6	0.4	5.8	0.5	2.7	0.14	2.8	0.2
Mn9	2.80E−06	2.35E−07			0.60	4.8	0.4			0.74	0.04		
Mn11	2.92E−06	2.46E−07	−1.30	0.12	0.61	–	–	–	–	0.00	–	0.0	–
Mn12	2.70E−06	2.27E−07	−1.44	0.11	0.61	4.5	0.3	4.6	0.4	0.80	0.04	0.80	0.06
Mn13	3.38E−07	2.84E−08	−1.39	0.15	0.63	14.0	1.1	15.3	1.4	63.31	3.23	65.4	4.6
Mg2	2.67E−06	2.24E−07	−1.44	0.15	0.42	–	–	0.018	0.002	–	–	0.23	0.02
Mg3	8.74E−07	1.31E−07	−1.35	0.14	0.42	–	–	0.028	0.002	–	–	3.31	0.23
Mg4	2.77E−06	2.33E−07	−1.35	0.11	0.57	–	–	0.024	0.002	–	–	0.030	0.002
Mg5	1.89E−06	1.59E−07	−1.40	0.13	0.44	–	–	0.022	0.002	–	–	1.34	0.09
Mg7†	2.50E−07	2.10E−08	−1.35	0.14	0.42	–	–	0.032	0.003	–	–	7.6	0.3

*Here, error refers to the analytical uncertainty. **Fraction of the bulk solid represented by (Me,Ca)CO_3 overgrowth. [a]Mn partitioning calculated from the growth solution data exclusively (Eq. (2.7)). [b]Mn partitioning calculated from the measured solid overgrowth composition (Section 2.4). †Aragonite is observed in the highest Mg experiment (Section 3.2.2).

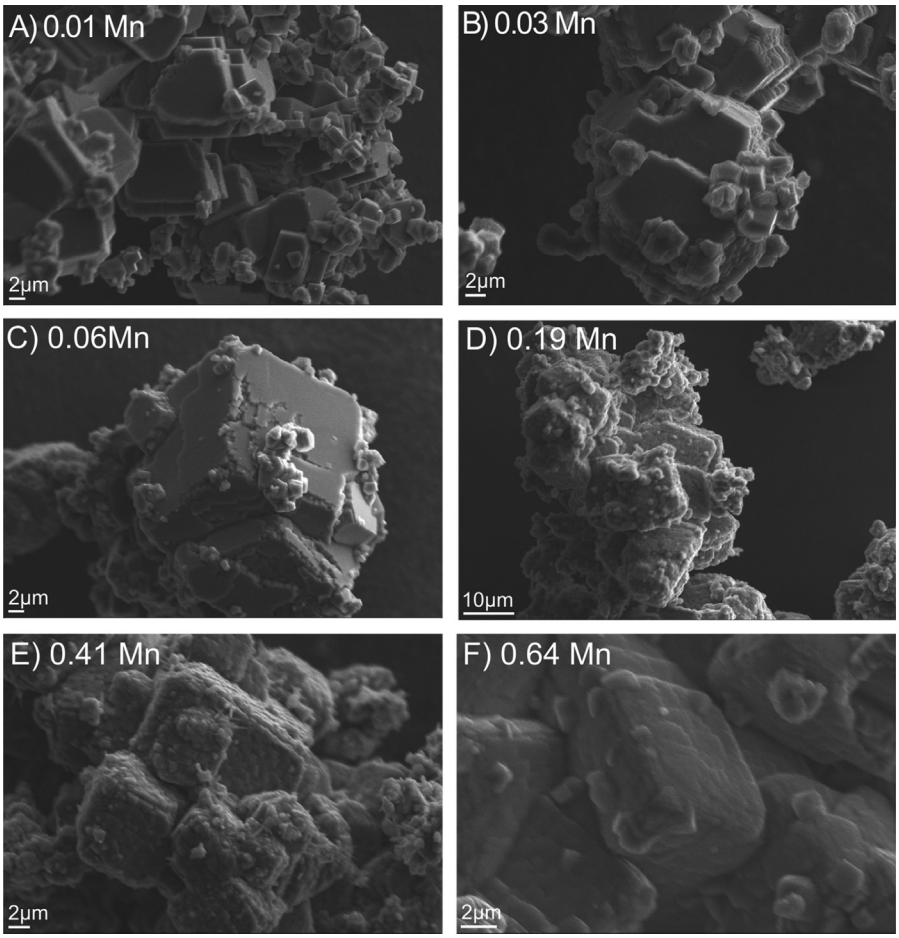

Fig. 2. High-magnification SEM images of growth features on precipitated (Mn,Ca)CO_3. Labeling denotes mole fraction $MnCO_3$ in the overgrowth. A) Mn12; B) Mn8; C) Mn3; D) Mn7; E) Mn5; F) Mn13.

curve was observed after ~20 h of growth (20 of 28 mL titrated), likely indicative of aragonite nucleation late in the experiment. The implications of this aragonite formation for data interpretation are discussed in the following section.

3.2. Precipitation of (Mn,Ca)CO_3 and (Mg,Ca)CO_3 solid solutions

3.2.1. (Ca,Mn)CO_3 series powder XRD results

Powder XRD results for the Mn^{2+} inhibition experiments are shown in Fig. S7. The calcite seed material produces pure-calcite peaks in all diffractograms. For overgrowths containing >6% $MnCO_3$, separated (Mn,Ca)CO_3 peaks shifted to higher 2θ are present, reflecting the decrease in d-spacing with substitution of the smaller Mn^{2+} ion for Ca^{2+}. The progressive shift in the rhombohedral carbonate 104 peak between calcite and rhodochrosite endmembers is highlighted in Fig. S7B and quantified in Fig. S8B. As the Mn content of the overgrowth increases, the 2θ of the 104 peak increases linearly but no separate rhodochrosite phase is detected. Observed shifts in the overgrowth 104 and 110 d-spacing (Fig. S8A,B) were used to calculate the a and c hexagonal unit cell parameters for the (Mn,Ca)CO_3 solid solutions precipitated (Fig. S8C,D).

The changes in unit cell parameters with solid Mn content observed here are in excellent agreement with the lattice parameter-Mn content relationships reported in previous calorimetric studies ((Capobianco and Navrotsky, 1987; Katsikopoulos et al., 2009), Fig. S8C, D). The linear decline in unit cell length with increasing Mn content (Vegard's law) and close agreement between the solid composition derived from chemical analysis and changes in lattice parameters observed in other studies where the Mn-calcites were synthesized through different methods (including high-temperature recrystallization (Capobianco and Navrotsky, 1987)) suggest that dominantly homogeneous calcite-rhodochrosite solid solutions were precipitated in this study. Notably, the (Mn,Ca)CO_3 overgrowth peaks do exhibit some level of peak broadening (Fig. S7). The full width half max (FWHM) of the pure calcite 104 peak is ~0.14° while comparable peaks for the well-separated (Mn,Ca)CO_3 overgrowth solid solutions exhibit FWHMs between 0.2 and 0.28°. This peak broadening could represent a degree of compositional heterogeneity or ordering in the lattice, but may also arise due to lattice strain effects or changes in crystallite size (Mittemeijer

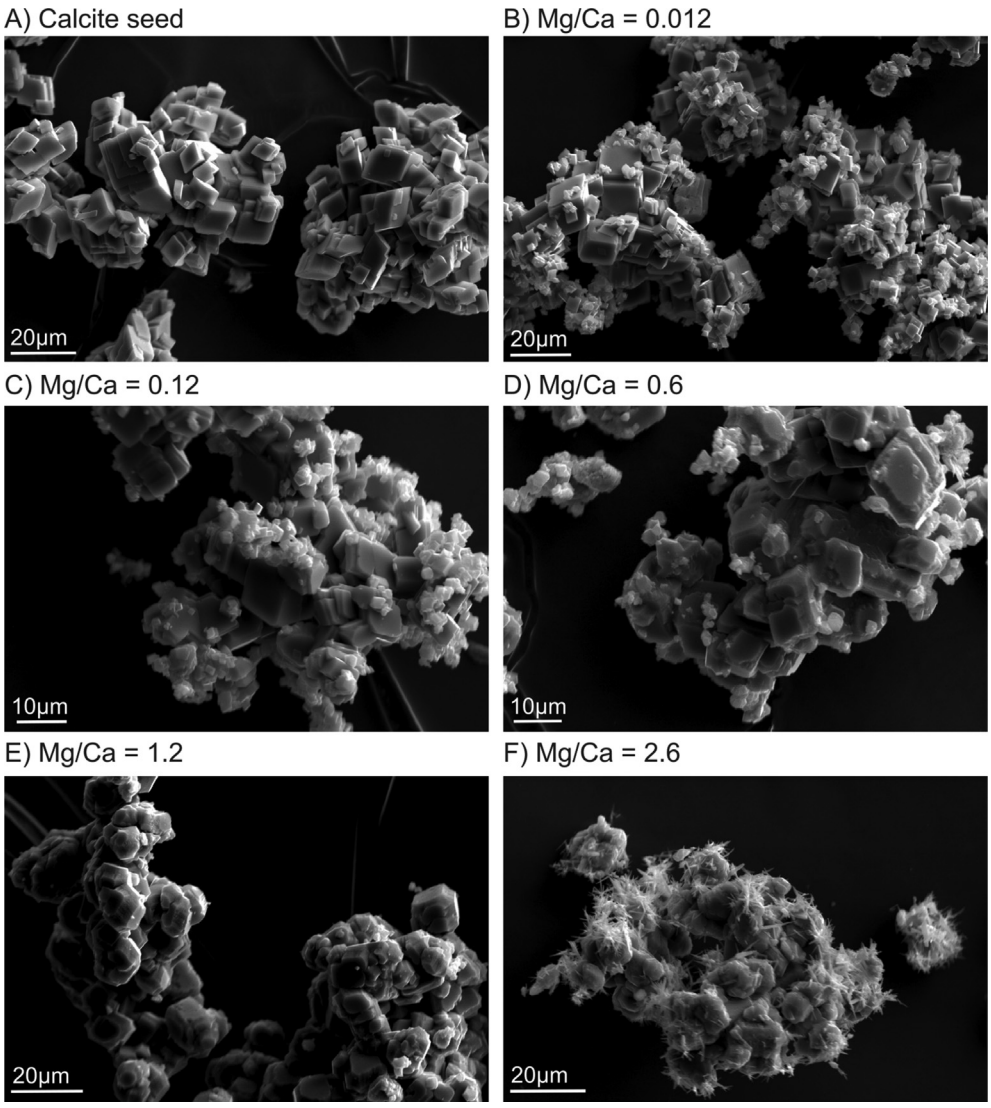

Fig. 3. Post-growth SEM images of precipitated solids from Mg^{2+} calcite inhibition experiments. Labeling denotes solution $\{Mg^{2+}\}/\{Ca^{2+}\}$. A) calcite seed material; B) Mg4; C) Mg2; D) Mg5; E) Mg3; F) Mg7.

and Welzel, 2008). The high-Mn experiments were run for a longer duration to achieve the same turnover of the Ca reservoir for Ca isotope analysis (Section 2.5), likely resulting in more nucleation of small $(Mn,Ca)CO_3$ particles. The surface texturing observed in the higher Mn content samples ($\geq$19% $MnCO_3$, Fig. 2) could also represent small crystallite domains. Higher resolution spatial analysis (e.g. HR-TEM) could help determine the cause and implications of the observed peak broadening.

3.2.2. *(Ca,Mg)CO_3 series powder XRD results*

Powder XRD results for the Mg^{2+} inhibition experiments are shown in Fig. S9. For experiments Mg2-Mg5, the Mg content of the overgrowth was too low (mol % Mg $\leq$ 3.3) to detect separated $(Mg,Ca)CO_3$ peaks (S9A). The magnesian-calcite overgrowth is visible in the diffractogram for the highest Mg experiment (Mg7, $\{Mg^{2+}\}/\{Ca^{2+}\}$ = 2.6) as separated peaks shifted to higher 2θ, in addition a clear aragonite phase (S9B,C). As discussed in Section 3.1, a change in slope of the titration curve after ~20 h of growth and SEM evidence of aragonite needles formed on the exterior of clusters of Mg-calcite crystals point towards aragonite nucleation later in the experiment. Both Reitveld refinement and Reference Intensity Ratio (RIR) phase quantification indicate that approximately 19% of the bulk solid is aragonite, equivalent to 38% of the overgrowth. We thus do not use bulk chemical analysis as the primary constraint on the Mg content of the calcite overgrowth for experiment Mg7. Instead, the composition is calculated from the d-spacing of the magnesian calcite 104 and 110 peaks, employing the lattice parameter - Mg content relationships for inorganic calcite developed by Bischoff et al. (1983):

$$a = 4.9906 - 0.50x + 0.56x^2 \quad (3.1)$$

$$c = 17.069–2.27x + 2.1x^2 \quad (3.2)$$

$$c/a = 3.420–0.118x + 0.05x^2 \quad (3.3)$$

where x is the mole fraction $MgCO_3$. The average x derived from the a, c, and c/a relationships yields a mole fraction $MgCO_3$ of 0.076 ± 0.003, thereby providing an estimate of Mg partitioning independent of the nucleated aragonite. We also include and interpret the growth rate calculated for Mg7 as the rate is calculated in the beginning stages of the experiment (5–10 mL titrated, Section 2.3), before the titration data indicate probable aragonite nucleation. The presence of aragonite has the most significant impact on our interpretation of the calcium isotope fractionation results. We calculate $\Delta^{44/40}Ca_{calcite\text{-}fluid}$ assuming a constant fractionation throughout the course of an experiment (Section 2.5), yielding an integrated fractionation representative of the Ca isotope discrimination during both the aragonite and magnesian calcite precipitation. Larger magnitude Ca isotope fractionations are often observed during aragonite precipitation than calcite precipitation at a given temperature, particularly for biomineralized carbonates (Gussone et al., 2005; Blättler et al., 2012). But recent inorganic precipitation experiments reported largely indistinguishable $\Delta^{44/40}Ca_{calcite\text{-}fluid}$ and $\Delta^{44/40}Ca_{aragonite\text{-}fluid}$, though the aragonite was generally grown at a slower rate, (AlKhatib and Eisenhauer, 2017a). The Ca isotope fractionate-rate trend observed in the inorganic aragonite growth experiments of Gussone et al. (2003) also overlaps with that observed in the inorganic calcite growth experiments of Tang et al. (2008) and Mills et al. (2021) for rates in the ~10^{-6}–10^{-7} mol/m^2/s regime (Fantle and Tipper, 2014). It is thus not clear whether the nucleated aragonite would be expected to exhibit a measurably different Ca isotope fractionation than the magnesian calcite of interest here, so the Mg7 calcium isotope data is interpreted with caution (Section 3.5).

3.3. Growth rate inhibition

Both Mn^{2+} and Mg^{2+} strongly inhibit calcite growth (Fig. 4). In the Mn experiments, log-linear rate inhibition is observed at low fluid Mn^{2+} concentrations; growth rates decline by almost an order of magnitude by $\{Mn^{2+}\}/\{Ca^{2+}\} = 0.02$ (Fig. 4A). With increasing solution Mn^{2+}, the extent of inhibition begins to asymptote and eventually reverses. For $\{Mn^{2+}\}/\{Ca^{2+}\} > 0.1$, faster growth rates are

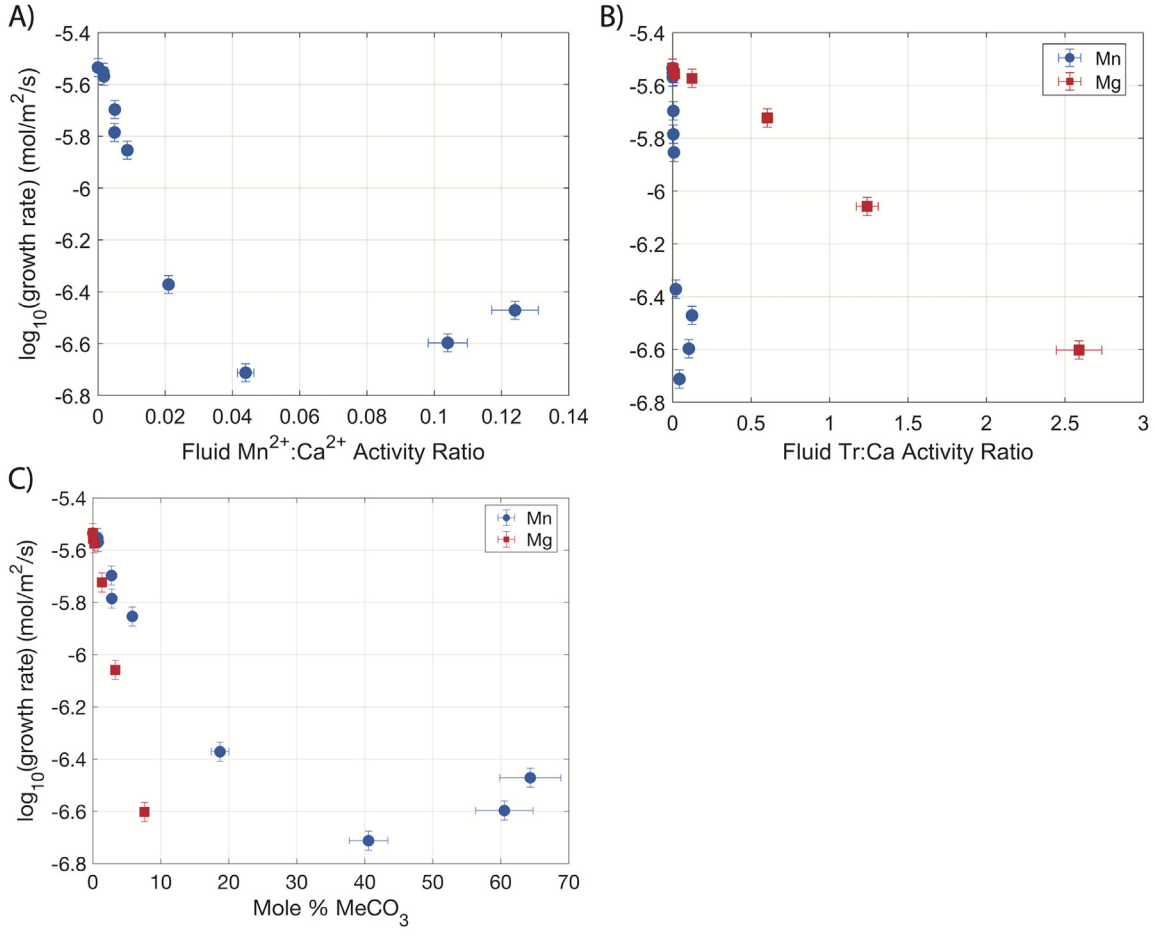

Fig. 4. Calcite growth rate inhibition by $Mn^{2+}$and Mg^{2+}. A) Surface-normal growth rate as a function of solution $\{Mn^{2+}\}/\{Ca^{2+}\}$. B) Data from A (blue circles) plotted alongside comparable growth rate data for Mg^{2+} (red squares). C) Surface-normal growth rates as a function of $(Me,Ca)CO_3$ solid composition. (For interpretation of the references to colour in this figure legend, the reader is referred to the web version of this article.)

observed with increasing solution Mn^{2+}. This growth rate inversion occurs when the Mn content of the precipitating solid surpasses approximately 40–50 mol %, transitioning into the regime of Ca-rich rhodochrosite solid solutions (Fig. 4C). Log-linear rate inhibition is also observed in the presence of Mg^{2+} but 100x higher inhibitor concentrations are required to achieve the same level of inhibition (Fig. 4B). Thus for the solution chemistries studied here, Mn^{2+} is a far stronger inhibitor of calcite growth than Mg^{2+} when viewed from the perspective of inhibitor concentration in solution. However, when considering the amount of inhibitor ion incorporated into the lattice, Mg^{2+} exhibits higher levels of rate inhibition per mole incorporated (Fig. 4C).

3.3.1. Temporal evolution of growth rate in high-Mn solutions

While the growth rate data reported in Fig. 4 reflect steady-state growth rates, in high-Mn solutions, the steady-state growth rate was not reached immediately. Instead, initial growth rates were markedly slower than the eventual steady-state growth rate and evolved to that rate over the first 0–1 mL titrated (Fig. S10). Moreover, the magnitude of the apparent additional inhibition at the start of the experiment scaled with Mn concentration: Higher $\{Mn^{2+}\}/\{Ca^{2+}\}$ experiments exhibited slower growth rates at the onset of the experiment (0–1 mL titrated) relative to their steady-state growth rate. These slow initial rates are observed for experiments where post-growth SEM images reveal a surface texturing reminiscent of rounded surface nuclei (Fig. 2C-E). This is potentially consistent with the in-situ AFM observations of Astilleros et al. (2002) who report a complete cessation of step advancement once the original calcite surface has been coated by a monolayer of $(Mn,Ca)CO_3$ in high-Mn solutions and a transition to 2D-nucleation driven growth. Higgins and Hu (2005) observe a similar phenomenon for Mg-calcite growth on dolomite surfaces, and attribute slow growth rates in the *second* monolayer deposited to the formation of a highly strained initial monolayer. The initial slow growth rates observed here could thus represent impaired growth kinetics as 2D surface nuclei must form on a strained epitaxial layer of high-Mn solid solutions deposited on the pure calcite seed surface.

3.4. Trace element partitioning

Mn^{2+} inhibition of calcite growth is accompanied by a strong, kinetically controlled, concentration of Mn in the calcite lattice (Fig. 5A,B). Large positive partition coeffi-

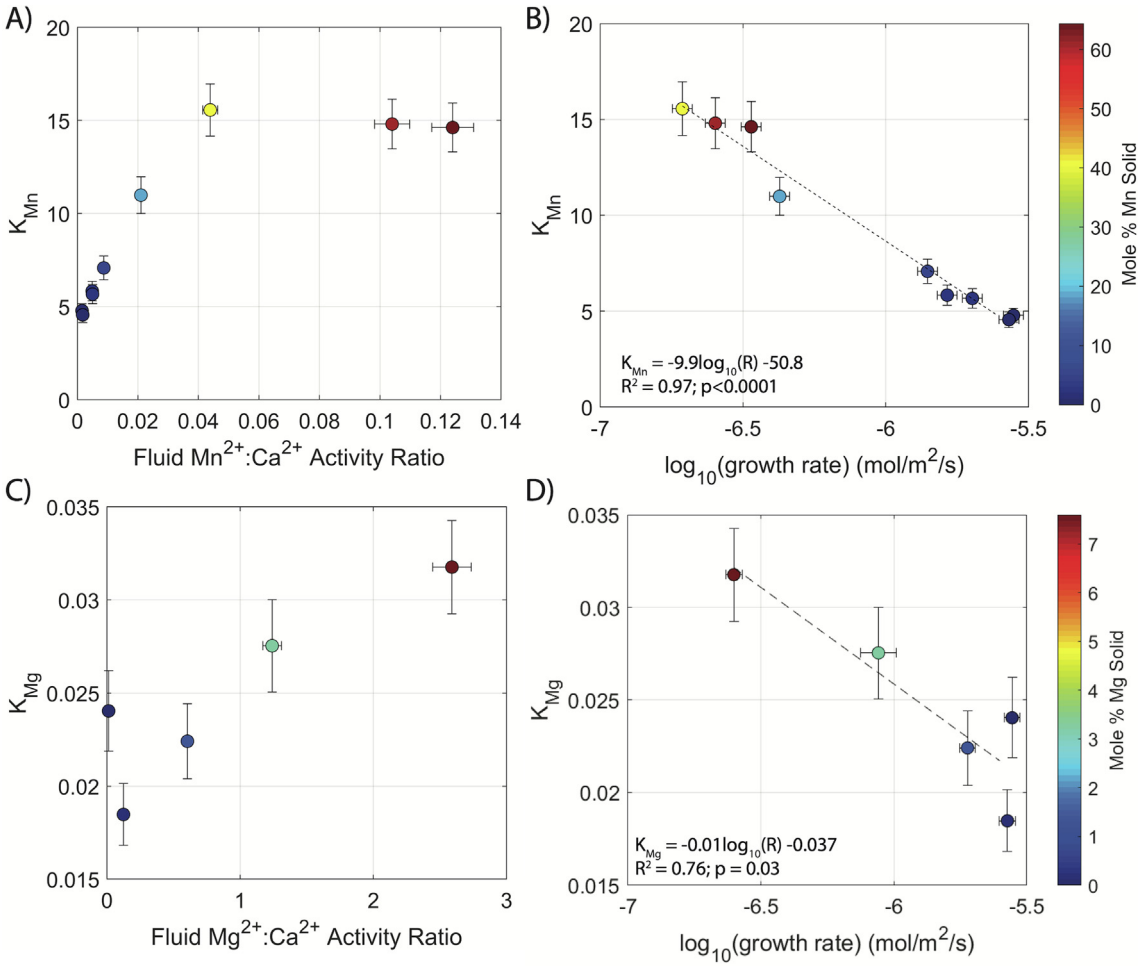

Fig. 5. Mn^{2+} and Mg^{2+} partition coefficients as a function of solution $\{Me^{2+}\}/\{Ca^{2+}\}$ (A,C) and growth rate (B,D).

cients (K_{Mn} = 4–16) are observed at low solution $\{Mn^{2+}\}/\{Ca^{2+}\}$, and K_{Mn} increases with increasing Mn^{2+} until $\{Mn^{2+}\}/\{Ca^{2+}\} = 0.044$ (Fig. 5A). Following the growth rate inversion observed when the precipitating solid solution exceeds 50 mol % $MnCO_3$ (Fig. 4C), K_{Mn} ceases to rise with increasing solution Mn^{2+}, instead plateauing and even slightly declining to a value of ~15. This yields a strong log-linear inverse correlation between K_{Mn} and growth rate, with the largest partition coefficients observed in the slowest growing, most highly inhibited, experiments (Fig. 5B). In contrast, the highly incompatible Mg^{2+} exhibits partition coefficients on the order of 0.02–0.03 (Fig. 5C,D). The data do not support an exceptionally strong dependence of partitioning on $\{Mg^{2+}\}/\{Ca^{2+}\}$ and thus growth rate for the solution conditions studied here; while K_{Mg} tends to increase with increasing $\{Mg^{2+}\}/\{Ca^{2+}\}$, most of the variability falls within the measurement uncertainty.

3.5. Ca isotope fractionation

Calcium isotope fractionation is found to be largely invariant across all solution conditions examined here (Fig. 6). In the presence of either Mn^{2+} or Mg^{2+}, large magnitude calcium isotope fractionations ($\Delta^{44/40}Ca_{calcite\text{-}fluid}$ = −1.3 to −1.44‰) are maintained, independent of $\{Me^{2+}\}/\{Ca^{2+}\}$ and associated kinetic inhibition. For both Mn^{2+} or Mg^{2+}, slightly larger magnitude fractionations are observed at low $\{Me^{2+}\}/\{Ca^{2+}\}$ than inhibitor-free solutions and $\Delta^{44/40}Ca$ trends back towards the pure-calcite endmember with increasing $\{Me^{2+}\}/\{Ca^{2+}\}$.

Interestingly, nearly identical $\Delta^{44/40}Ca$ is observed in experiment Mg7, despite the precipitation of aragonite (Fig. 6B, red asterisk). As discussed in Section 3.2.2, up to 40% of the precipitated solid may be aragonite, which is generally thought to exhibit larger magnitude Ca isotope fractionations. The comparable $\Delta^{44/40}Ca$ observed here suggests either that aragonite and Mg-calcite fractionate Ca isotopes similarly under these solution conditions (as discussed above (Fantle and Tipper, 2014; AlKhatib and Eisenhauer, 2017a)) or that a larger magnitude aragonite fractionation could obscure a somewhat smaller magnitude $\Delta^{44/40}Ca_{calcite\text{-}fluid}$. The measured fractionation for Mg7 is thus considered a maximum estimate, but in the absence of unequivocal evidence to the contrary, we continue under the assumption that $\Delta^{44/40}Ca_{calcite\text{-}fluid}$ is independent of $\{Mg^{2+}\}/\{Ca^{2+}\}$.

4. DISCUSSION

4.1. Mn and Mg kinetic data

Both Mn^{2+} and Mg^{2+} exhibit log-linear rate inhibition of calcite growth at low $\{Me^{2+}\}/\{Ca^{2+}\}$, with 100x stronger inhibition by Mn^{2+} when viewed from the perspective of fluid inhibitor concentration. Importantly, at higher Mn^{2+} concentrations ($\{Mn^{2+}\}/\{Ca^{2+}\} > 0.04$), the inhibition begins to plateau and growth rates eventually begin to increase with added Mn^{2+} while Mg^{2+} maintains a log-linear inhibition trend to high $\{Mg^{2+}\}/\{Ca^{2+}\}$. This is consistent with previous observations of Mg^{2+} inhibition of calcite growth. Davis et al. (2000b) observe a log-linear decline in step velocities and bulk growth rate up to a $\{Mg^{2+}\}/\{Ca^{2+}\}$ of 2 and Astilleros et al. (2010) report continued inhibition up to $\{Mg^{2+}\}/\{Ca^{2+}\} = 5$.

The inhibition observed here can be directly compared to kinetic data from previous studies by examining how the extent of inhibition varies as a function of solution chemistry. The extent of inhibition is defined as $(R_0\text{-}R)/R_0$, where R_0 is the pure calcite growth rate under otherwise comparable solution conditions. Fig. 7A and C compare the extent of calcite growth inhibition as a function of $\{Me^{2+}\}/\{Ca^{2+}\}$ for Mn^{2+} and Mg^{2+}, respectively, for bulk growth studies that were performed at similar supersaturations with respect to calcite. The inhibition behavior documented here is in very good agreement with previous

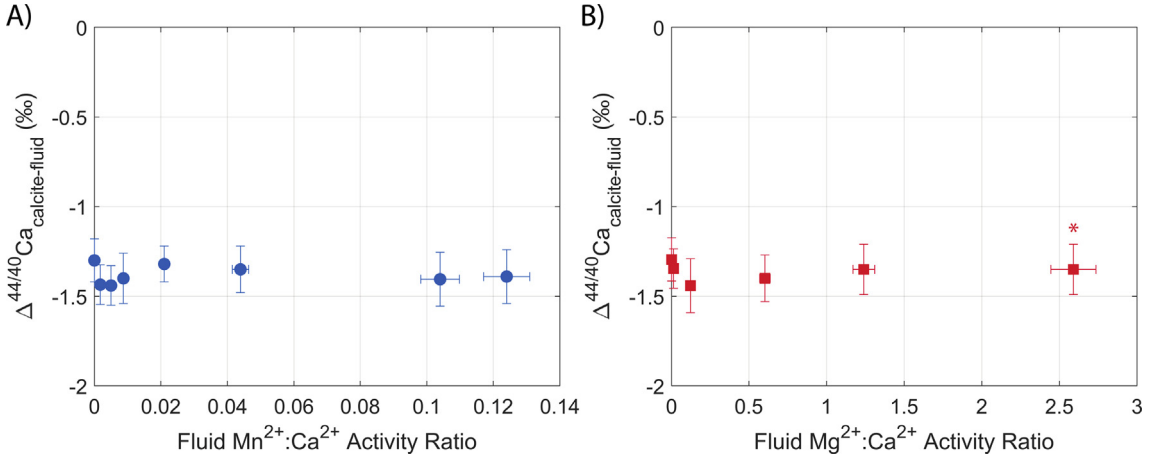

Fig. 6. Calcium isotope fractionation during Mn^{2+} and Mg^{2+} inhibition of calcite growth. Note, experiment Mg7 ($\{Mg^{2+}\}/\{Ca^{2+}\} = 2.6$, noted by a red asterisk above the marker) contains aragonite as well as Mg-calcite in the overgrowth. See main text for discussion of implications for interpretation. (For interpretation of the references to colour in this figure legend, the reader is referred to the web version of this article.)

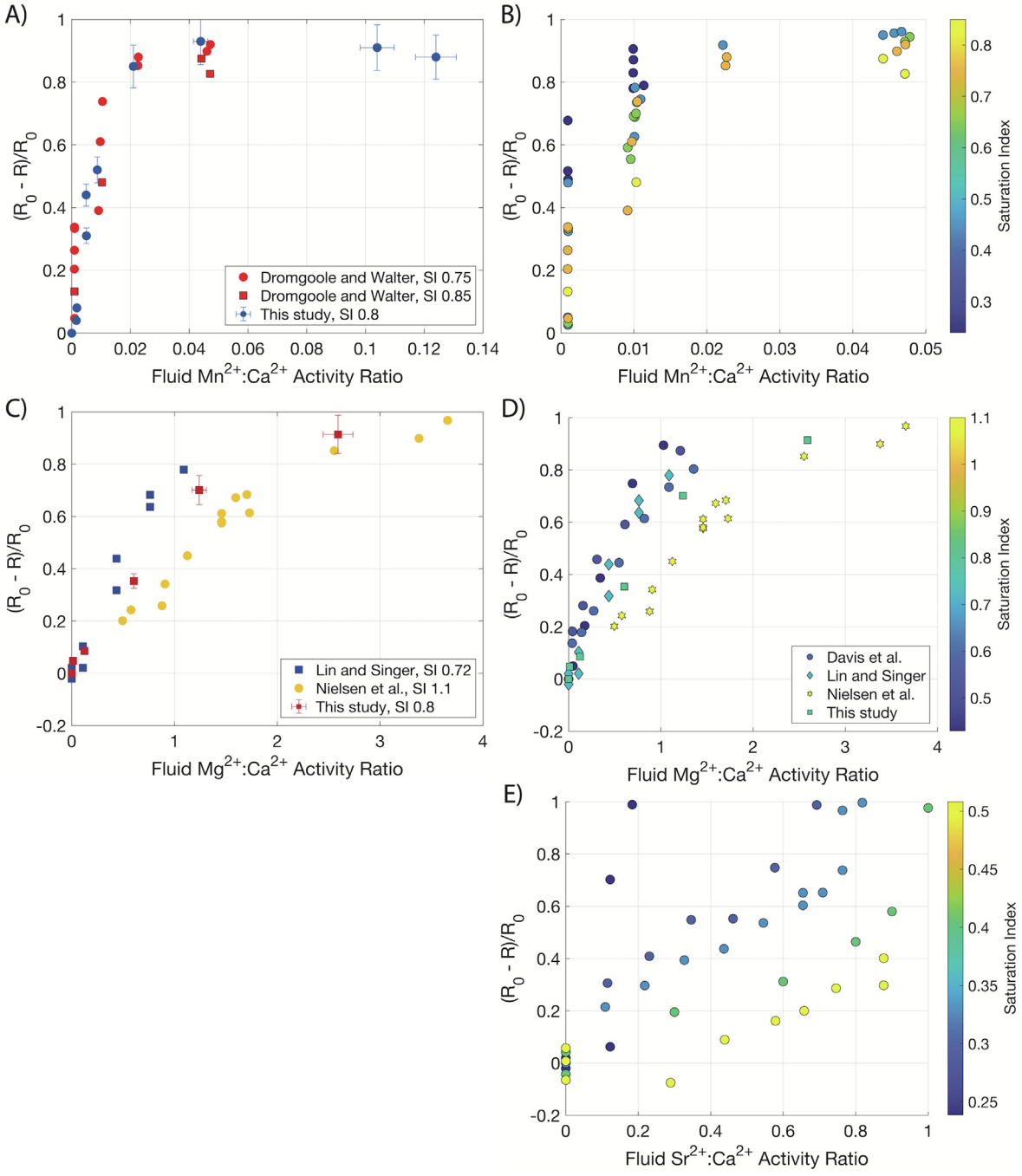

Fig. 7. Extent of calcite growth inhibition across studies and inhibitor systems. A) Extent of inhibition as a function of $\{Mn^{2+}\}/\{Ca^{2+}\}$ observed in this study and similar SI bulk growth experiments from Dromgoole and Walter (1990a). B) Data from Dromgoole and Walter (1990a), segmented by SI range, demonstrating higher extent of inhibition for a given $\{Mn^{2+}\}/\{Ca^{2+}\}$ at lower SI. C) Extent of inhibition as a function of $\{Mg^{2+}\}/\{Ca^{2+}\}$ observed in this study and similar SI bulk growth experiments from Lin and Singer (2009) and Nielsen et al. (2016). D) Literature compilation of Mg^{2+} bulk growth rate inhibition data, segmented by SI. A higher extent of inhibition is observed in lower SI solutions both within individual studies (Davis et al., 2000b) and across studies (Davis et al., 2000b; Lin and Singer, 2009; Nielsen et al., 2016). E) Comparable extent of inhibition data for calcite inhibition by Sr^{2+} from Wasylenki et al. (2005a), showing much higher sensitivity to SI.

findings, despite differences in solution chemistry. In particular, the extensive experiments of Dromgoole and Walter (1990a) confirm that calcite growth is highly inhibited at very low solution Mn^{2+}($\{Mn^{2+}\}/\{Ca^{2+}\} < 0.02$) but that inhibition begins to plateau at higher $\{Mn^{2+}\}/\{Ca^{2+}\}$ as calcian rhodochrosite starts to form (Fig. 7A). Similarly for Mg^{2+}, the inhibition behavior observed here falls between the data of Lin and Singer (2009) and Nielsen et al. (2016), which were performed at lower and higher supersaturations than this study, respectively (Fig. 7C).

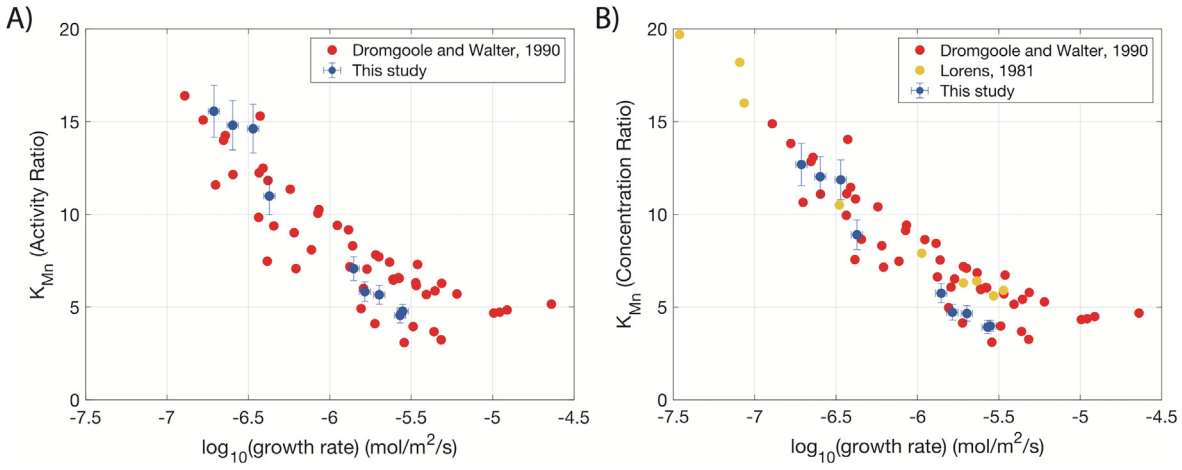

Fig. 8. Mn^{2+} partitioning into calcite exhibits a strong log-linear inverse dependence on growth rate across a wide range of solution conditions. K_{Mn} calculated using solution activity ratio (A) and concentration ratio (B) vs. growth rate for data from this study, Dromgoole and Walter (1990a), and Lorens (1981). Note, only data from experiments performed in milli-Q water from Lorens (1981) are included. See Table 3 for a summary of solution conditions used in each study.

Table 3
Solution conditions for Mn^{2+} and Mg^{2+} partitioning studies.

Experiment	SI	$\{Me^{2+}\}/\{Ca^{2+}\}$	pH	$\{Ca^{2+}\}/\{CO_3^{2-}\}$	Ionic strength
Mn^{2+} studies					
This study	0.8	0.001–0.14	8.0	110	0.1 M KCl
Dromgoole and Walter, 1990a	0.3–1.0	0.001–0.05	~6	10^3-10^5	~0.3 M
Lorens (1981)	~0.1–0.8	$\sim10^{-10}$	7.5	300–1400	0.7 M NaCl
Mg^{2+} studies					
This study	0.8	0.01–2.6	8.0	110	0.1 M KCl
Mavromatis et al. (2013)	0.1–0.5	0.2–1.4	~6.2	10^3-10^4	0.1–0.6 M NaCl
Nielsen et al. (2016)	0.8	0.5–3.5	8.3	~50	0.1 M NaCl

These findings highlight another trend not evident from this study alone: both Mn^{2+} and Mg^{2+} inhibition of calcite growth are supersaturation dependent (Fig. 7B,D). Lower supersaturation solutions exhibit a higher extent of inhibition for a given $\{Me^{2+}\}/\{Ca^{2+}\}$, a trend that has been documented by numerous other studies (Mucci and Morse, 1983; Dromgoole and Walter, 1990a; Davis et al., 2000a). This supersaturation sensitivity is particularly strong at low $\{Mn^{2+}\}/\{Ca^{2+}\}$ during the log-linear inhibition phase (Fig. 7B). That said, the magnitude of the supersaturation dependence observed for Mn^{2+} and Mg^{2+} is considerably lower than that observed for Sr^{2+} ((Wasylenki et al., 2005a), Fig. 7E). Sr^{2+} was interpreted to inhibit calcite growth through a dominantly solid solution thermodynamic effect by Nielsen et al. (2013). This observed dependence between supersaturation and growth rate inhibition thus represents a testable prediction for ground-truthing mechanistic interpretations in the ion-by-ion framework (Section 4.4).

4.2. Mn and Mg incorporation dynamics

4.2.1. Mn partitioning

The Mn^{2+} partitioning trend observed here demonstrates a strong inverse relationship between K_{Mn} and growth rate (Figs. 5, 8). K_{Mn} increases with increasing $\{Mn^{2+}\}/\{Ca^{2+}\}$ during the log-linear growth rate inhibition phase, then plateaus and even declines, mirroring the plateau in rate inhibition and growth rate inversion observed when the mole fraction Mn in the solid solution exceeds ~0.5. This inverse dependence between K_{Mn} and growth rate holds over a wide range of solution conditions. Fig. 8 shows the partitioning data from this study, plotted alongside data from Dromgoole and Walter (1990a) and Lorens (1981); solution conditions for the three studies are summarized in Table 3. The comprehensive suite of experiments of Dromgoole and Walter (1990a) targeted a similar range in $\{Mn^{2+}\}/\{Ca^{2+}\}$ to that investigated in this study, but were run at a significantly lower pH and thus higher $\{Ca^{2+}\}/\{CO_3^{2-}\}$. In contrast, Lorens (1981) investigated Mn^{2+} partitioning using radioactive ^{54}Mn, thereby achieving solution conditions with orders of magnitude lower $\{Mn^{2+}\}/\{Ca^{2+}\}$ than traditional bulk-growth studies (Table 3).

Despite these differences, all the partitioning data fall along the same log-linear rate trend (Fig. 8). This is consistent with the surface kinetic model developed by DePaolo (2011), where trace element partitioning (like stable isotope fractionation) varies between kinetic and equilibrium

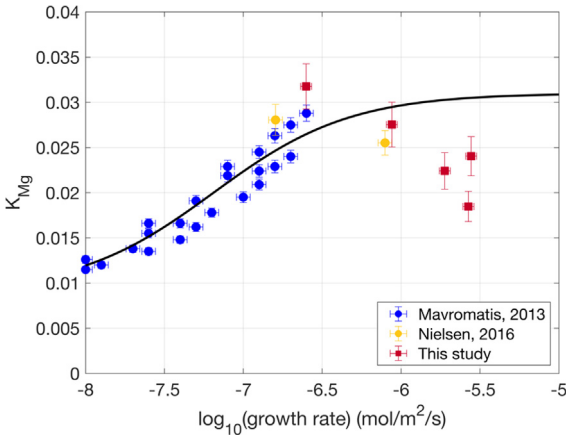

Fig. 9. Literature compilation of Mg^{2+} partitioning results. The results from this study (red squares) and Nielsen et al. (2016) depart from the strong log-linear trend observed by Mavromatis et al. (2013). Notably, the Mavromatis et al. (2013) experiments were run at a much lower pH and thus higher $\{Ca^{2+}\}/\{CO_3^{2-}\}$; see Table 3 for a summary of solution conditions. The DePaolo (2011) model prediction of K_{Mg} is shown as a solid black line (see text for discussion). (For interpretation of the references to colour in this figure legend, the reader is referred to the web version of this article.)

endmembers, dictated by the degree of exchange occurring at the surface:

$$K_{Me} = \frac{K_f}{1 + \frac{R^b}{R^f}\left(\frac{K_f}{K_{eq}} - 1\right)} \quad (4.1)$$

where K_f is the forward kinetic fractionation factor for Me/Ca in the forward precipitation reaction; K_{eq} is the equilibrium partition coefficient; and R^b, R^f are the back and forward precipitation fluxes (the net growth rate, $R^p = R^f - R^b$ where R^b is assumed to be 6e-7 mol/m^2/s based on the calcite dissolution study of Chou et al. (1989)). In this simplified framework, the Mn^{2+} partitioning data across studies is consistent with an equilibrium partition coefficient of ~55 and kinetic endmember of 4, the lowest value observed here. Although we will explore this partitioning in greater detail using the full mechanistic ion-by-ion model in Section 4.4.1, the common trend observed here highlights that Mn^{2+} partitioning is highly kinetically controlled. Mn^{2+} partitioning and calcite growth rate respond to solution conditions in a remarkably consistent manner.

4.2.2. Mg partitioning

In contrast to the highly consistent partitioning-growth rate trend observed for Mn^{2+} among different studies, comparing Mg^{2+} partitioning data across studies reveals a marked divergence in the relationship between K_{Mg} and growth rate (Fig. 9). While the dataset of Mavromatis et al. (2013) exhibits a strong positive correlation between K_{Mg} and rate, where higher partition coefficients are observed at faster rates, the K_{Mg} measured in this study and the similar bulk-growth study of Nielsen et al. (2016) depart from that trend. However, the three datasets overlap in the $10^{-6.5}$-10^{-7} mol/m^2/s growth rate regime, making it unclear whether they represent a single trend with a rate inversion at ~$10^{-6.5}$-10^{-7} mol/m^2/s or if fundamentally different rate dependencies are observed under different solution conditions. A single dataset that spans the $10^{-5.5}$ to $10^{-7.5}$ mol/m^2/s growth rate range under controlled solution conditions is required to definitively interpret these Mg^{2+} partitioning observations, but we explore some potential explanations here.

First we consider the possibility that the datasets represent fundamentally different K_{Mg}-rate behaviors. The experiments of Mavromatis et al. (2013) were run at lower pH, higher $\{Ca^{2+}\}/\{CO_3^{2-}\}$, and lower supersaturation than used in this study and Nielsen et al. (2016) (Table 3), so the deviation from the positive log-linear trend could represent a pH or supersaturation effect. Mucci and Morse (1983) report a trend of declining K_{Mg} with increasing $\{Mg^{2+}\}/\{Ca^{2+}\}$ and declining growth rate in seawater solutions (pH 7.7–8.2, SI 0.6–1.2), in line with the Mavromatis et al. (2013) trend. In contrast, Gabitov et al. (2014) found that K_{Mg} declines with increasing growth rate in a study of Mg^{2+} partitioning into single calcite crystals grown in NH_4Cl solutions (pH ~8, SI ~0.3).

Another possibility stems from the observation that Mavromatis et al. (2013) did not report any changes in calcite morphology following the precipitation of their magnesian calcite overgrowths, in contrast to the rounded and elongated crystal forms observed here at elevated $\{Mg^{2+}\}/\{Ca^{2+}\}$ (Section 3.1). The inverse rate dependence observed here may instead be driven by differences in preferential Mg^{2+} interaction with specific faces (Reeder and Grams, 1987; Zhang and Dawe, 2000) or steps on the $(10\bar{1}4)$ surface (Paquette and Reeder, 1995; Davis et al., 2004). In particular, the experiments in this study are run with a KCl background electrolyte (0.1 M ionic strength) while the Nielsen et al. (2016) and Mavromatis et al. (2013) studies were run in NaCl, with a total ionic strength of 0.1 M and 0.1–0.6 M, respectively. Importantly, in NaCl solutions, the obtuse calcite step propagates substantially faster (2-4x) than the acute step while roughly equal obtuse/acute step velocities are observed in KCl solutions (Ruiz-Agudo et al., 2011; Stephenson et al., 2011; Hong and Teng, 2014). Stephenson et al. (2011) also report that increasing ionic strength suppresses Mg^{2+} uptake in a background electrolyte-specific manner. It is thus possible that the trend of increasing K_{Mg} with increasing $\{Mg^{2+}\}/\{Ca^{2+}\}$ observed here stems from the background electrolyte used; perhaps relatively more Mg^{2+} is incorporated into the lattice at high $\{Mg^{2+}\}$ in KCl solutions because there is less interaction between the 'background' electrolyte and the acute calcite step where Mg^{2+} is preferentially incorporated.

Finally, as discussed in more detail in the Supplementary Information (S1.1), in the ion-by-ion model framework, the slope of the K_{Mg}-$\{Mg^{2+}\}/\{Ca^{2+}\}$ relationship is sensitive to assumptions regarding calcite-magnesite solid solution thermodynamics. Lower values of the W_{12} parameter in the sub-regular solid solution model yield increasing K_{Mg} with $\{Mg^{2+}\}/\{Ca^{2+}\}$ as observed here while higher values yield the opposite relationship as observed by Mavromatis et al. (2013) and Mucci and Morse (1983)

((Lammers and Mitnick, 2019), Fig. S17). Ordering has been shown to strongly influence the excess enthalpy of mixing for both Mg^{2+} (Navrotsky and Capobianco, 1987; Burton and Van de Walle, 2003; Lammers and Mitnick, 2019) and Mn^{2+} (Wang et al., 2011). Different levels of Mg/Ca ordering within the calcite lattice could conceivably influence the K_{Mg}-$\{Mg^{2+}\}/\{Ca^{2+}\}$ and thus rate relationship.

It is also possible that the data from this study, Mavromatis et al. (2013), and Nielsen et al. (2016) all represent a cohesive trend in K_{Mg} vs. growth rate. Again working from the DePaolo (2011) surface kinetic framework (Eq. (4.1)), in order to achieve a plateau in the K_{Mg} vs. rate relationship at $\sim 10^{-6.5}$ mol/m^2/s as observed, R^b must be a factor of 30x slower than that assumed from calcite dissolution studies (Chou et al., 1989; DePaolo, 2011). A low Mg^{2+} back flux (equivalently, Mg^{2+} detachment rate) is consistent with observations that the far from equilibrium dissolution rate for magnesite is between 100 and 1000x slower than that of calcite under a wide range of conditions (Chou et al., 1989; Pokrovsky et al., 2009). Fig. 9 shows predicted K_{Mg}, assuming R^b = 1.88e-8 mol/m^2/s, K^f = 0.031, andK^{eq} = 0.0089. Note that this model does not explain all of the observed partitioning behavior: Nothing in the DePaolo (2011) framework can predict the decline in K_{Mg} observed at faster rates in our experiments. But a plateau in K_{Mg} at $\sim 10^{-6.5}$ mol/m^2/s is qualitatively consistent with the Nielsen et al. (2016) experiments run with a NaCl background electrolyte and the DePaolo (2011) surface kinetic framework hints that this may be explained in part due to slow Mg removal from the calcite surface. As further explored using the ion-by-ion modeling framework in Section 4.4.3, a sluggish Mg removal flux is consistent with other observations, including the supersaturation sensitive inhibition behavior described above (Section 4.1). We thus posit that slow Mg^{2+} detachment from the calcite surface may contribute to the observed apparent inconsistencies between Mg^{2+} partitioning datasets, but again caution that additional data is required from a single cohesive dataset that spans the $10^{-5.5}$ to $10^{-7.5}$ mol/m^2/s growth rate range to further elucidate these observations.

4.3. Invariant $\Delta^{44/40}$Ca supports kink-blocking inhibition mechanism

Inorganic calcite growth experiments performed in the absence of inhibitors exhibit an inverse, log-linear relationship between calcium isotope fractionation and growth rate (Tang et al., 2008; Mills et al., 2021). The invariant $\Delta^{44/40}$Ca during calcite inhibition by Mg^{2+} and Mn^{2+} draws the fractionations observed here off the pure calcite $\Delta^{44/40}$Ca-rate relationship, with high magnitude fractionations maintained despite more than an order of magnitude decline in growth rate (Fig. 10). Mills et al. (2021) experimentally verified the conceptual framework of calcium isotope discrimination driven by Ca exchange at kink sites during growth. The invariant $\Delta^{44/40}$Ca thus indicates that calcite growth inhibition by Mg^{2+} and Mn^{2+} does not change the *relative* rates of Ca addition vs. removal from kink sites. As discussed above, this is consistent with kink-blocking type inhibition, where the inhibitor dominantly influences the rates of ion attachment at kink sites and subsequent kink propagation kinetics but does not substantially destabilize the calcite lattice, which would increase the back flux of Ca (Mills et al., 2021).

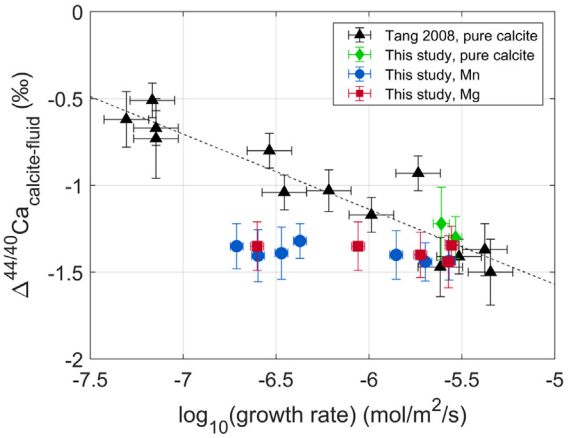

Fig. 10. Invariant $\Delta^{44/40}$Ca with $\{Me^{2+}\}/\{Ca^{2+}\}$ draws observed fractionations off the pure calcite $\Delta^{44/40}$Ca -growth rate relationship and suggests that Mn^{2+} and Mg^{2+} inhibit calcite growth through a dominantly kink-blocking mechanism. Data from the Mn^{2+} (blue circles) and Mg^{2+}(red squares) experiments are plotted alongside data from inhibitor-free inorganic calcite growth experiments: 25 °C dataset from Tang et al. (2008) (black triangles with linear regression shown as the dotted line) and $\{Ca^{2+}\}/\{CO_3^{2-}\}$ = 100, SI = 0.8 data from the current study and Mills et al. (2021). (For interpretation of the references to colour in this figure legend, the reader is referred to the web version of this article.)

Kink blocking inhibition is consistent with slow inhibitor cation desolvation kinetics, as has been proposed by Astilleros et al. (2010) and Nielsen et al. (2013) for the case of Mg^{2+}. The smaller Mg^{2+} ion is much more strongly hydrated than Ca^{2+}, and the water exchange frequency for Mg^{2+} is >3 orders of magnitude lower than that of Ca^{2+} (Helm and Merbach, 1999). Magnesium may thus inhibit calcite growth by attaching at kink sites and literally blocking their propagation because it is slow to shed its hydration waters, impeding both Mg^{2+} attachment at the kink and subsequent CO_3^{2-} attachment at Mg^{2+}-occupied kinks.

While Mn^{2+} should also dehydrate more slowly than Ca^{2+}, with an approximately 1 order of magnitude lower water exchange frequency (Helm and Merbach, 1999), it should shed its hydration waters faster than Mg^{2+}. Thus, despite the nearly identical behavior in $\Delta^{44/40}$Ca as a function of growth rate and similar log-linear inhibition observed at low a $\{Mn^{2+}\}/\{Ca^{2+}\}$, it is difficult to explain the much stronger inhibition by Mn^{2+} at low solution inhibitor concentrations in terms of cation-desolvation rate-limited kink blocking alone. Moreover, the strong partitioning of Mn^{2+} into calcite (indicated by $K_{Mn} > 1$) is inconsistent with an Mn attachment flux controlled entirely by monomer ion desolvation kinetics.

Table 4
Model parameters for Mn^{2+} inhibition of calcite growth. *Following Katsikopoulos et al. (2009).

Ca^{2+} kinetic parameters				
	k_{Ca} ($s^{-1}M^{-1}$)	k_{CO3} ($s^{-1}M^{-1}$)	$v_{Ca,0}$ (s^{-1})	$v_{CO3,0}$ (s^{-1})
	3.75e6	2.2e7	523	523
Mn^{2+} kinetic parameters				
Mechanism	k_{Mn} ($s^{-1}M^{-1}$)	$k_{CO3,Mn}$ ($s^{-1}M^{-1}$)	$v_{Mn,0}$ (s^{-1})	$v_{CO3\ Mn,0}$ (s^{-1})
Cation desolvation driven kink blocking	0.001*k_{Ca}	1e-5*k_{Ca}	4.5e-4	0.002
Complex addition + carbonate kink blocking	12*k_{Ca}	0.033*k_{Ca}	3	13.6
Solid solution thermodynamic parameters				
Guggenheim parameters	a_0	a_1	a_2	K_{sp}, $MnCO_3$*
	1.5	−1.1	0	$10^{-11.13}$
Endmember calcium isotope fractionations				
	α_f	0.9967	α_{eq}	0.9995

4.4. Insights from ion-by-ion modeling

In searching for a mechanistic driver for calcite inhibition by Mg^{2+} and Mn^{2+}, several observations must be explained. First, Mn^{2+} is an ~100x stronger inhibitor of calcite growth than Mg^{2+} but exhibits a similar log-linear inhibition trend at low $\{Mn^{2+}\}/\{Ca^{2+}\}$. Second, inhibition by both Mn^{2+} and Mg^{2+} is sensitive to supersaturation, and a higher extent of inhibition is observed at lower supersaturation for a given $\{Me^{2+}\}/\{Ca^{2+}\}$. Third, large positive Mn^{2+} partition coefficients are observed at low $\{Mn^{2+}\}/\{Ca^{2+}\}$, and K_{Mn} is strongly inversely correlated to growth rate. Fourth, K_{Mg} is on the order of 0.02–0.03 and increases with $\{Mg^{2+}\}/\{Ca^{2+}\}$ over the solution conditions studied here. Fifth and finally, the $\Delta^{44/40}Ca$ is invariant with $\{Mn^{2+}\}/\{Ca^{2+}\}$ and $\{Mg^{2+}\}/\{Ca^{2+}\}$ despite more than an order of magnitude decline in growth rate. In the following sections we employ the ion-by-ion model of Nielsen et al. (2013) to explore the mechanistic implications of this suite of observations. The details of the model as used here are provided in Supplementary Information (S1).

4.4.1. Mn inhibition of calcite growth: Evidence for non-monomer incorporation

For Mn^{2+} inhibition of calcite growth, the first inhibition mechanism that can be categorically ruled out is cation desolvation-driven kink blocking. Fig. S11 shows modeled growth rate, K_{Mn}, and $\Delta^{44/40}Ca$ as a function of solution $\{Mn^{2+}\}/\{Ca^{2+}\}$ for growth inhibition driven by slow attachment of Mn^{2+} at CO_3^{2-} kink sites and CO_3^{2-} at Mn^{2+} kink sites (Table 4). To achieve the level of inhibition observed at low $\{Mn^{2+}\}/\{Ca^{2+}\}$, Mn^{2+} addition must be so slow that virtually no manganese is incorporated into the calcite lattice (Fig. S11B). Thus, although kink blocking driven by sluggish Mn^{2+} attachment kinetics is consistent with the invariant $\Delta^{44/40}Ca$ observed (Fig. S11C), the large positive K_{Mn} at low $\{Mn^{2+}\}/\{Ca^{2+}\}$ observed rules out an incorporation mechanism that is rate-limited by Mn^{2+} desolvation at kink sites.

To capture the Mn^{2+} incorporation behavior observed, Mn^{2+} must attach substantially *faster* than Ca^{2+} such that $k_{Mn} \gg k_{Ca}$ (Table 4). This behavior strongly suggests that desolvation kinetics is not the factor controlling Mn incorporation, as Mn^{2+} exhibits slower desolvation kinetics than Ca^{2+} (Helm and Merbach, 1999). This, in turn, suggests that the attaching species is either charge-neutral, which would be the case if it were an ion pair, or a larger polynuclear cluster. This is consistent with the findings of Sternbeck (1997), who described rhodochrosite growth kinetics in terms of $MnCO_3^0$ addition to surface sites, and observations of the influence of carbonate ion concentration on Mn^{2+} interaction with the calcite surface during dissolution under far from equilibrium conditions (Vinson et al., 2007). Vinson et al. (2007) invoke $MnCO_3^0$ complex formation and the associated reduction in the barrier to cation dehydration and surface attachment as a key component of Mn^{2+} inhibition of calcite dissolution. But considering that the rapid Mn^{2+} attachment still leads to growth inhibition, there must be some slow component of the attachment process. We hypothesize that this slow process involves the carbonate ion as discussed further below. Independent of the specific model, the data offer clear evidence for a novel hybrid classical/nonclassical growth pathway wherein Mn primarily incorporates as a non-monomer species, while Ca incorporates and exchanges as free Ca^{2+}.

The observed Mn^{2+} attachment/inhibition behavior can be accounted for by making appropriate adjustments to the exchange rate constants in the ion-by-ion calcite growth model. Fig. 11 shows modeled growth rate, K_{Mn}, and $\Delta^{44/40}Ca$ as a function of solution $\{Mn^{2+}\}/\{Ca^{2+}\}$ for a scenario where Mn^{2+} readily attaches at the calcite surface ($k_{Mn} = 12\ k_{Ca}$) and growth inhibition is driven by slow attachment of CO_3^{2-} at Mn^{2+} kink sites (Table 4). This mechanism captures both the magnitude of growth rate inhibition and manganese partitioning, while predicting very little change in $\Delta^{44/40}Ca$ with increasing $\{Mn^{2+}\}/\{Ca^{2+}\}$. The Mn^{2+} partitioning behavior, in particular the shape of the K_{Mn}-$\{Mn^{2+}\}/\{Ca^{2+}\}$ relationship (Fig. 11B)

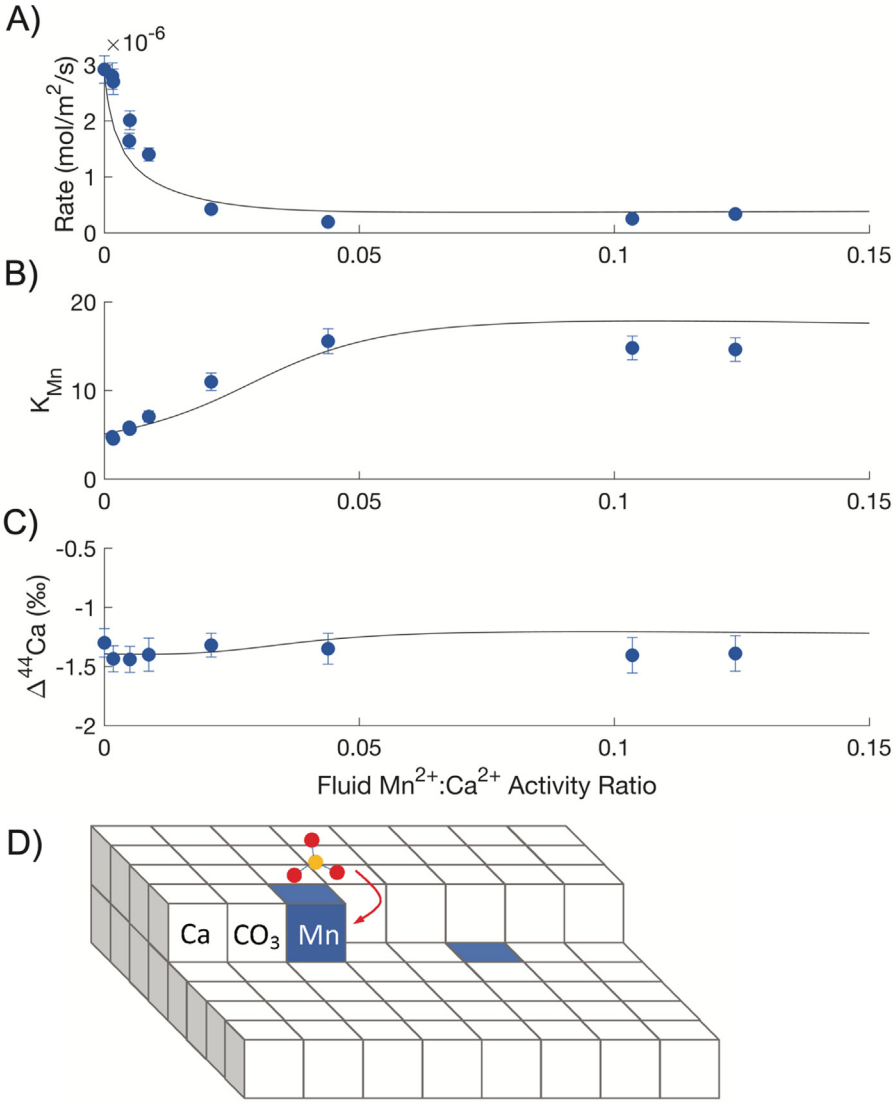

Fig. 11. Ion-by-ion model prediction (solid black line) of bulk growth rate (A), Mn partition coefficient (B), and $\Delta^{44/40}Ca_{calcite\text{-}fluid}$ (C) as a function of $\{Mn^{2+}\}/\{Ca^{2+}\}$ for Mn^{2+} inhibition of calcite growth driven by Mn^{2+} complex addition (allowing for $k_{Mn} \gg k_{Ca}$) coupled to kink-blocking due to slow CO_3^{2-} attachment at Mn^{2+} kink sites. See Table 4 for model parameters. D) Schematic of proposed carbonate based kink-blocking mechanism: slow re-orientation kinetics of carbonate ions that have formed an inner-sphere complex with Mn^{2+} at the surface but must reorient to incorporate into the lattice.

is highly sensitive to assumptions regarding calcite-rhodochrosite solid solution thermodynamics (Supplementary Information, S1). We find the partitioning trends observed here are best described with an excess free energy of mixing with positive deviations from ideality, close but not identical to the calorimetric measurements of Katsikopoulos et al. (2009) and Capobianco and Navrotsky (1987) (Fig. S12). Notably, the model does predict a slight decrease in the magnitude of $\Delta^{44/40}Ca$ at higher $\{Mn^{2+}\}/\{Ca^{2+}\}$, as Ca is destabilized in the lattice (v_{Ca} increases) at intermediate $(Mn,Ca)CO_3$ solid solution compositions. While we do not measure more positive $\Delta^{44/40}Ca$ values at high $\{Mn^{2+}\}/\{Ca^{2+}\}$, the stabilization of the solid solution implied by the increasing growth rates measured here at $\{Mn^{2+}\}/\{Ca^{2+}\} > 0.1$ suggests that the model may be slightly over-estimating the v_{Ca} increase at high $\{Mn^{2+}\}/\{Ca^{2+}\}$ for the solution conditions studied. At lower supersaturations, the model captures the growth rate inversion (Fig. 12), which would be associated with a trend back to slightly larger magnitude $\Delta^{44/40}Ca$.

4.4.2. Model for slow carbonate ion attachment

We propose that the apparent carbonate kink blocking could arise from slow re-orientation kinetics of carbonate ions that have formed an inner-sphere complex with Mn^{2+} at the surface but must rotate to incorporate into the lattice (Fig. 11D). Unlike the spherical cations, the planar carbonate molecule can only be incorporated into the calcite lattice when the C-O-C plane is perpendicular to the C-axis of calcite. Hong and Teng (2014) argued that

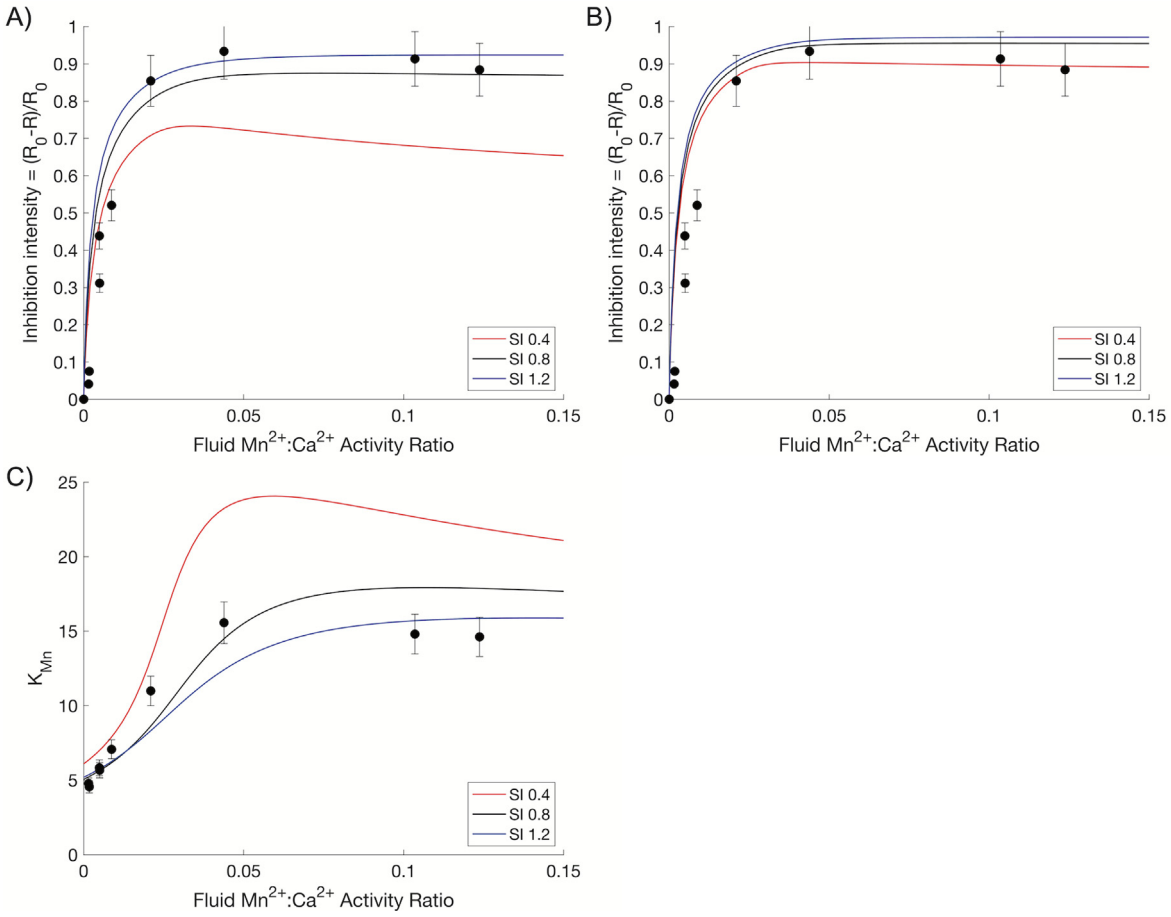

Fig. 12. Predicted sensitivity of Mn^{2+} growth rate inhibition and partitioning to supersaturation. A) Predicted extent of inhibition as a function of fluid $\{Me^{2+}\}/\{Ca^{2+}\}$ for different supersaturation solutions, using the solution chemistry studied here. B) As in A, but using a $\{Ca^{2+}\}/\{CO_3^{2-}\}$ ratio of 3e4, representative of the conditions studied by Dromgoole and Walter (1990a). C) Predicted Mn^{2+} partition coefficient as a function of fluid $\{Me^{2+}\}/\{Ca^{2+}\}$ for different supersaturation solutions, using the solution chemistry studied here. In all, model predictions are shown as solid lines.

the rate limiting step in the propagation of acute calcite steps is the surface adsorption and reorientation of CO_3^{2-} ions based on observations of the differential response of acute and obtuse steps to changes in pH and Ca^{2+}:CO_3^{2-} solution stoichiometry. Mn^{2+} also forms ion pairs in solution much more readily than Ca^{2+} or Mg^{2+}. Most estimates of the thermodynamic stability constant (logK) for the $MnCO_3^0$ ion pair formation reaction range from 4 to 5 (Langmuir, 1979; Turner et al., 1981; Wolfram and Krupp, 1996; Luo and Millero, 2003), while the logK's for Ca^{2+} and Mg^{2+} carbonate ion pair formation reactions are 3.2 (Plummer and Busenberg, 1982) and 2.9, respectively (Reardon and Langmuir, 1974). Thus, a potential mechanism for the inhibition observed here is that interaction with surface Mn^{2+}, concentrated on the acute steps (Paquette and Reeder, 1995), further inhibits carbonate ion reorientation and leads to severely impeded CO_3^{2-} attachment at Mn^{2+} kink sites.

The proposed inhibition mechanism is consistent with other observations (Sections 4.1, 4.2.1). First, examining how K_{Mn} varies with $\{Mn^{2+}\}/\{Ca^{2+}\}$ for a range of supersaturations (Fig. 12C), we find that larger partition coefficients are predicted for a given $\{Mn^{2+}\}/\{Ca^{2+}\}$ in lower supersaturation (and thus slower growth rate) solutions. This is consistent with the inverse correlation between K_{Mn} and growth rate (Fig. 8). Considering the sensitivity of inhibition to supersaturation, Fig. 12A shows the supersaturation dependence of the inhibition intensity for the solution conditions examined here. Unlike that observed by Dromgoole and Walter (1990a), a lower extent of inhibition is predicted at lower supersaturations for a given $\{Mn^{2+}\}/\{Ca^{2+}\}$. Notably, the Dromgoole and Walter (1990a) experiments were run at very high $\{Ca^{2+}\}/\{CO_3^{2-}\}$ (Table 3); implementing a comparably high $\{Ca^{2+}\}/\{CO_3^{2-}\}$ in the ion-by-ion model yields a lower sensitivity to supersaturation (Fig. 12B) but does not capture the trend of higher inhibition at lower supersaturations. Importantly, without in-situ AFM measurements, we have no indication of how the presence of Mn^{2+} influences hillock step spacing (y_0, Supplementary Information S1.2), leaving a key parameter in the scaling of modeled step velocities to bulk growth rates uncertain. A higher extent of inhibition at low $\{Mn^{2+}\}/\{Ca^{2+}\}$ for low supersaturation solutions could be driven by relatively larger changes

in y_0 with increasing $\{Mn^{2+}\}/\{Ca^{2+}\}$ at low supersaturation. Calcite inhibition by Sr^{2+} exhibits this pattern (Fig. S5). Wasylenki et al. (2005a) reported that y_0 increases by a factor of 3 between $\{Sr^{2+}\}/\{Ca^{2+}\} = 0$ and $\{Sr^{2+}\}/\{Ca^{2+}\} = 0.8$ in SI = 0.33 solutions, but y_0 only increases by a factor of 1.5 over a comparable range of $\{Sr^{2+}\}/\{Ca^{2+}\}$ in SI = 0.51 solutions. This leads to markedly stronger bulk growth rate inhibition than step velocity inhibition at lower supersaturations, particularly at low $\{Me^{2+}\}/\{Ca^{2+}\}$ where Mn^{2+} inhibition is also observed to be most sensitive to supersaturation (Fig. S5A,B).

If future measurements reveal that the trend in inhibition sensitivity to supersaturation observed by Dromgoole and Walter (1990a) cannot be explained by changes in step spacing, the model presented here would need to be critically re-evaluated to consider whether aspects of the model framework are more sensitive to supersaturation than currently assumed, or if the framework is missing fundamental processes such as 2D step nucleation inhibition. Most obviously, the inhibition mechanism proposed here requires Mn^{2+} to attach at kink sites as a non-monomer species, which is not considered in classical growth models but may be incorporated into process-based models. Expanding the ion-by-ion model to incorporate non-classical processes (Section 4.6) as well as exploring the implications of changes in growth mechanism due to the presence of inhibitors, for example a transition to 2D nucleation driven growth (Section 3.1) and step-specific strain effects (Davis et al., 2004; Hong et al., 2016), are important avenues for future work.

4.4.3. Mg inhibition of calcite growth: Mechanisms of kink-blocking

In contrast to Mn^{2+}, our observations of calcite growth inhibition by Mg^{2+} are mostly consistent with a classical cation desolvation driven kink blocking mechanism, but the model application points to additional complexities that we explore in detail here. Fig. 13 shows modeled growth rate, K_{Mg}, and $\Delta^{44/40}Ca$ as a function of solution $\{Mg^{2+}\}/\{Ca^{2+}\}$ for growth inhibition driven by slow attachment of Mg^{2+} at CO_3^{2-} kink sites and CO_3^{2-} at Mg^{2+} kink sites (Table 5, Scenario 1). The model captures the key characteristics of Mg^{2+} inhibition observed: log-linear rate inhibition that continues to high $\{Mg^{2+}\}/\{Ca^{2+}\}$; K_{Mg} on the order of 0.02–0.03 that increases with $\{Mg^{2+}\}/\{Ca^{2+}\}$; and constant $\Delta^{44/40}Ca$.

While the model captures the trends in rate inhibition, partitioning, and calcium isotope discrimination observed here, the predicted *extent* of inhibition exhibits the wrong supersaturation dependence (Fig. S15A). While observations both within single experiments (Davis et al., 2000b) and from across the literature (Fig. 7D) demonstrate that experiments run at a lower supersaturation are more strongly inhibited at a given $\{Mg^{2+}\}/\{Ca^{2+}\}$, the opposite

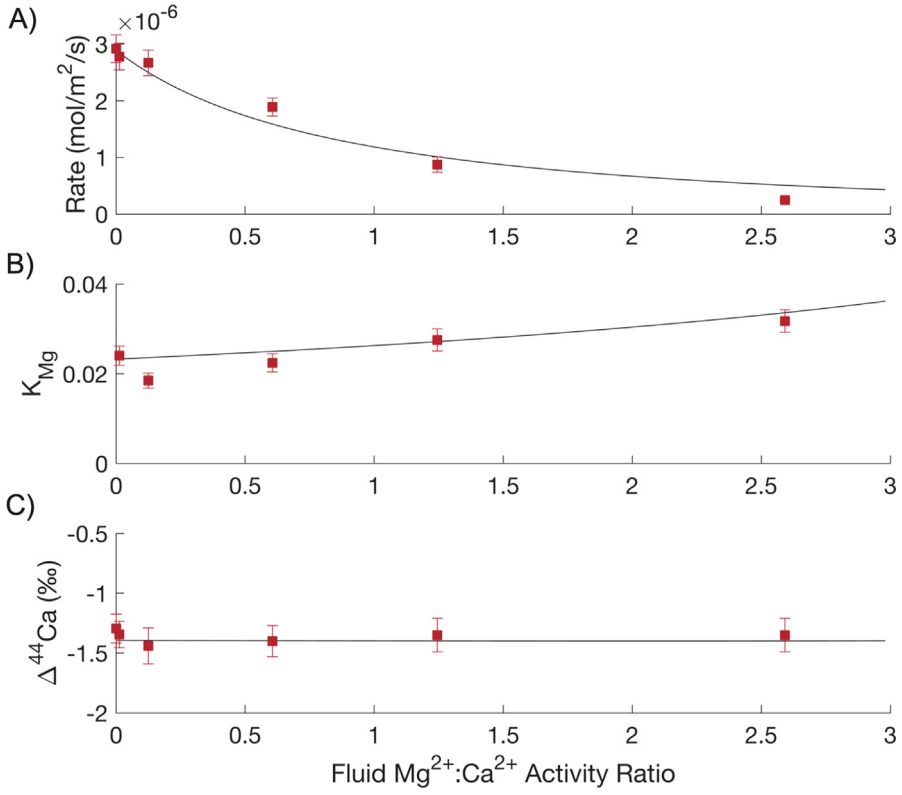

Fig. 13. Ion-by-ion model prediction (solid black line) of bulk growth rate (A), Mg partition coefficient (B), and $\Delta^{44/40}Ca_{calcite\text{-}fluid}$ (C) as a function of $\{Mg^{2+}\}/\{Ca^{2+}\}$ for Mg^{2+} inhibition of calcite growth driven by Mg^{2+}-solvation driven kink blocking. See Table 5 for model parameters (Scenario 1 with y_0 scaled to the observations of Davis et al. (2000a)).

Table 5
Model parameters for Mg^{2+} inhibition of calcite growth.* (Bénézeth et al., 2011).

Ca^{2+} kinetic parameters					
		k_{Ca} ($s^{-1}M^{-1}$)	k_{CO3} ($s^{-1}M^{-1}$)	$v_{Ca,0}$ (s^{-1})	$v_{CO3,0}$ (s^{-1})
		3.75e6	2.2e7	523	523
Mg^{2+} kinetic parameters: Cation desolvation driven kink blocking					
Scenario	y_0	k_{Mg} ($s^{-1}M^{-1}$)	$k_{CO3,\ Mg}$ ($s^{-1}M^{-1}$)	$v_{Mg,0}$ (s^{-1})	$v_{CO3\ Mg,0}$ (s^{-1})
1	thermo	$0.05*k_{Ca}$	$0.05*k_{Ca}$	8	1800
	Davis scaled	$0.2*k_{Ca}$	$0.2*k_{Ca}$	150	1500
2	thermo	$0.008*k_{Ca}$	$0.024*k_{Ca}$	0.001	0.001
	Davis scaled	$0.008*k_{Ca}$	$0.12*k_{Ca}$	0.01	1
3	Davis scaled	$0.025*k_{Ca}$	$0.125*k_{Ca}$	6	3000
Mg^{2+} kinetic parameters: Carbonate kink blocking					
Mechanism	y_0	k_{Mg} ($s^{-1}M^{-1}$)	$k_{CO3,\ Mg}$ ($s^{-1}M^{-1}$)	$v_{Mg,0}$ (s^{-1})	$v_{CO3\ Mg,0}$ (s^{-1})
Complex addition +	thermo	$15*k_{Ca}$	$0.0135*k_{Ca}$	1075	1075
carbonate kink blocking	Davis scaled	$5.5*k_{Ca}$	$0.055*k_{Ca}$	1300	1300
Solid solution thermodynamic parameters					
Interaction parameters	W_{12} (kJ/mol)	W_{21} (kJ/mol)	K_{sp}, $MgCO_3$*		
	8	8	$10^{-7.795}$		
Endmember calcium isotope fractionations					
		α_f	0.9967	α_{eq}	0.9995

trend is predicted in the version of the model depicted in Fig. 13. Within the ion-by-ion modeling framework employed here (Nielsen et al., 2013), the only mechanism we could identify that would both capture the measured data and predict stronger inhibition at lower supersaturation was cation-desolvation driven kink blocking, coupled to negligible Mg^{2+} detachment rates (Fig. S13, S15B; Table 5, Scenario 2). This was achieved in the ion-by-ion framework by disconnecting v_{Mg} from calcite-magnesite solid solution thermodynamics and dictating that $v_{Mg} \ll v_{Ca}$ (Table 5).

Sluggish Mg^{2+} detachment kinetics could be caused by kinetic constraints on Mg^{2+} hydration as it leaves the kink site and are potentially consistent with the 100-1000x slower dissolution rate of magnesite relative to calcite as previously discussed (Chou et al., 1989; Pokrovsky et al., 2009). However, forcing negligible Mg^{2+} detachment yields Mg partitioning behavior inconsistent with that observed in most studies (Fig. S16B). While all other mechanisms explored here exhibit higher K_{Mg} at higher solution supersaturations, consistent with the growth rate trend documented by Mavromatis et al. (2013), turning off Mg^{2+} detachment yields the opposite trend (Fig. S16B).

In reality, cation desolvation-driven kink blocking by Mg^{2+} would likely resemble something in between the endmember scenarios represented by scenarios 1 and 2 (Table 5), where v_{Mg} is low as suggested by the slow magnesite dissolution kinetics, but still linked to the solubility of the calcite lattice. This inhibition pathway is depicted by scenario 3 (Fig. S14), achieved in the ion-by-ion framework by assuming that $\nu_{CO3,Mg} \gg \nu_{Mg}$ (Table 5). Assuming a low Mg^{2+} detachment flux leads to predicted growth rate inhibition that is largely insensitive to supersaturation (Fig. S15C) but Mg^{2+} partitioning that exhibits the supersaturation dependence observed by Mavromatis et al. (2013) (Fig. S16C). As will be discussed in more detail below, the lower sensitivity to inhibition in higher supersaturation solutions observed experimentally could be linked to processes not accounted for in the ion-by-ion framework such as incomplete dehydration of Mg^{2+} at faster growth rates, so we avoid making mechanistic deductions based on the inhibition supersaturation dependence alone.

We have thus far demonstrated that our observations of Mg-calcite precipitation dynamics can be captured by an ion-by-ion model of calcite growth in which growth is limited by Mg^{2+} desolvation kinetics. Assuming Mg^{2+} also exhibits slow detachment kinetics from kink sites brings the modeled inhibition supersaturation sensitivity closer to that observed experimentally. However, the inhibition and partitioning behavior observed here can *also* be captured by a carbonate kink blocking mechanism similar to that invoked for Mn^{2+}. As with Mn^{2+}, a Mg^{2+} attachment rate faster than that of Ca^{2+} must be invoked in this scenario, which is physically implausible if the species interacting with the calcite surface is a free Mg^{2+} ion in solution that is required to fully dehydrate before attaching at a CO_3^{2-} kink site. Fig. 14 shows modeled growth rate, K_{Mg}, and $\Delta^{44/40}Ca$ as a function of solution $\{Mg^{2+}\}/\{Ca^{2+}\}$ for growth inhibition driven by fast attachment of Mg^{2+}, coupled to slow CO_3^{2-} attachment at Mg^{2+} kink sites, potentially due to slow surface dehydration of Mg^{2+}. Using a step width that increases with $\{Mg^{2+}\}/\{Ca^{2+}\}$ following the observations of Davis et al. (2000a), Mg^{2+} must attach a factor of 5.5x faster than Ca^{2+}, and CO_3^{2-} must attach a factor of 100x slower than Mg^{2+} (Table 5). This model scenario does an exceptionally good job of capturing the bulk growth rate inhibition observed here (Fig. 14A).

While faster attachment of Mg^{2+} than Ca^{2+} is inconsistent with free Mg^{2+} in solution needing to fully dehydrate before attaching at a CO_3^{2-} kink site, slow CO_3^{2-} attachment on Mg^{2+} kinks is consistent with recent atomistic simulations that emphasize the likelihood of exceptionally slow

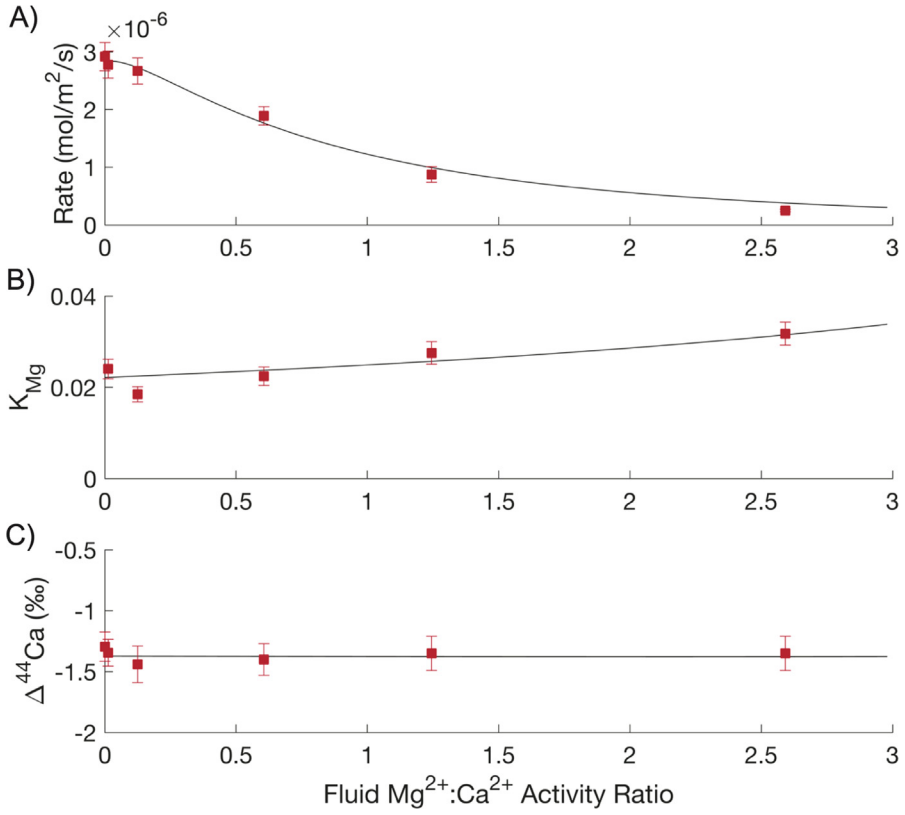

Fig. 14. Ion-by-ion model prediction (solid black line) of bulk growth rate (A), Mg partition coefficient (B), and $\Delta^{44/40}Ca_{calcite\text{-}fluid}$ (C) as a function of $\{Mg^{2+}\}/\{Ca^{2+}\}$ for Mg^{2+} inhibition of calcite growth driven by Mg^{2+} complex addition and carbonate ion kink blocking. See Table 5 for model parameters (y_0 scaled to the observations of Davis et al. (2000a)).

Mg^{2+} dehydration on the calcite surface. In simulating the surface hydration dynamics of calcite, dolomite, and magnesite, Reischl et al. (2019) found that while Ca sites on the calcite surface exhibited a mean water residence time of ~2 ns, not a single exchange of a water molecule in the first hydration layer was observed over the Mg sites of dolomite or magnesite over a 200 ns long simulation. It is thus highly likely that at least part of the kink blocking inhibition indicated by the invariant $\Delta^{44/40}Ca$ is driven by slow CO_3^{2-} attachment on Mg^{2+} kinks due to surface dehydration rate limitation. In all scenarios investigated here, $k_{CO3,Mg}$ must be smaller than k_{Ca} by a factor of 5–100 (Table 5).

Regarding the possibility that Mg^{2+} could attach faster than Ca^{2+} (at least under some conditions), we turn to observations of Mg isotope fractionation during calcite growth. In inhibitor-free solutions, the magnitude of calcium isotope fractionation increases with increasing growth rate (Fig. 10). This trend is echoed by stable Sr^{2+} (AlKhatib and Eisenhauer, 2017b) and Ba^{2+} (von Allmen et al., 2010; Mavromatis et al., 2020) fractionation during calcite precipitation. In contrast, both Mg^{2+} (Immenhauser et al., 2010; Mavromatis et al., 2013) and Ni^{2+} (Alvarez et al., 2021) exhibit the opposite trend, with the largest magnitude fractionations measured at the slowest growth rates (Fig. S18). Though it should be noted that other studies of Mg isotope fractionation during calcite growth find $\Delta^{26}Mg$ to be independent of calcite growth rate (Chen et al., 2020). Like Mg^{2+}, Ni^{2+} is considerably more strongly hydrated than Ca^{2+}; the water exchange frequency for the Ni^{2+}-aquo ion is 5 orders of magnitude slower than that of Ca^{2+}. Mavromatis et al. (2013) and Alvarez et al. (2021) interpret this rate dependence to represent the progressive incorporation of more hydrated Mg^{2+} species at faster growth rates, working from the premise that the incorporation of incompletely dehydrated cations would lead to substantially less isotope discrimination. This argument could be expanded to include the incorporation of Mg-complexes more broadly, as density functional theory calculations suggest that the heavy ^{26}Mg isotope partitions preferentially into aqueous Mg-carbonate complexes (Schott et al., 2016).

This raises the possibility that at least some portion of Mg^{2+} is incorporated as a partially hydrated or otherwise complexed species and that the proportion of complexed Mg^{2+} increases with precipitation rate. It is important to emphasize that the current ion-by-ion model does not explicitly allow for this possibility; the incorporation of only one single Mg^{2+} species is considered. Thus the 'carbonate kink blocking' scenario modeled in Fig. 14 does not represent the variably hydrated impurity cation mechanism proposed by Mavromatis et al. (2013) and Alvarez et al. (2021) but instead exemplifies an endmember scenario in which all Mg^{2+} attaches rapidly at carbonate kink sites in the absence of the kinetic barrier of complete Mg^{2+}-aquo

complex dehydration. Notably, the supersaturation dependence of inhibition predicted by this model scenario is again opposite to that observed experimentally (Fig. 7D vs. S15D). However, if the Mg^{2+} and Ni^{2+} isotope trends are truly indicative of higher levels of partially hydrated cation incorporation at faster growth rates, this also has important ramifications for the supersaturation dependence of inhibition by Mg^{2+}. For a given $\{Mg^{2+}\}/\{Ca^{2+}\}$, in lower supersaturation solutions we would expect that a smaller proportion of Mg^{2+} is incorporated as a hydrated species, meaning that the full kink-blocking potential of Mg^{2+} is expressed. Kink propagation is inhibited by slow Mg^{2+} desolvation of both the aquo-complex and the subsequent Mg^{2+} kink site. But at the faster growth rates experienced in higher supersaturation solutions, the incorporation of partially hydrated Mg^{2+} circumvents the kinetic bottleneck of aquo-complex desolvation, leading to lower levels of rate inhibition. Thus the incorporation of varying levels of partially hydrated Mg^{2+} could help explain the inhibition sensitivity to supersaturation observed experimentally (Fig. 7D).

In all, the experimental observations and modeling undertaken here demonstrate that Mg^{2+} inhibits calcite growth through a dominantly kink-blocking mechanism, but that mechanism is likely not as simple as 'the Mg^{2+}-aquo complex dehydrates slowly relative to Ca^{2+}'. Instead, this likely represents one endmember scenario, seen in Mg-calcite growth at low supersaturations and net precipitation rates, where the kink-blocking potential of Mg^{2+} is fully expressed. Kink propagation is limited by Mg^{2+} desolvation both during cation attachment and subsequent desolvation of the Mg^{2+} kink site for CO_3^{2-} attachment. But under other solution conditions, Mg^{2+} desolvation during attachment at kink sites may not be kinetically limiting due to the incorporation of partially hydrated or otherwise complexed Mg^{2+}. This would lessen the extent of inhibition and magnitude of Mg^{2+} isotope discrimination, but calcite growth would remain significantly inhibited by the kinetics of CO_3^{2-} attachment at Mg^{2+} kink sites. Further elucidation of the nuances of this inhibition mechanism will require a combination of molecular modeling, studies of paired isotope measurements under controlled solution conditions, and extension of our kinetic modeling frameworks to explicitly allow for non-monomer impurity incorporation (Section 4.6).

4.5. Implications for interpretation of $\Delta^{44/40}Ca$ in natural systems

There is significant interest in using measurements of $\delta^{44/40}Ca$ in sedimentary carbonations to reconstruct the isotopic and chemical characteristics of the precipitating fluid (Fantle and Tipper, 2014). This requires knowledge of how various aspects of solution chemistry dictate the magnitude of calcium isotope fractionation as well as a broader understanding of the geochemical context in which the minerals were precipitated, including the influence of biomineralization or biologically induced mineralization, closed vs. open-system behavior, and any subsequent recrystallization (Ahm et al., 2018; Higgins et al., 2018; Gussone et al., 2020). Mills et al. (2021) demonstrated that $\Delta^{44/40}Ca_{calcite\text{-}fluid}$ is less sensitive to solution stoichiometry than originally predicted, which lends more confidence to interpretations of calcite saturation state and associated growth rate from observed fractionations. Here we have demonstrated that inhibition of calcite growth through a dominantly kink-blocking mechanism does not measurably influence $\Delta^{44/40}Ca$. Indeed, for a given supersaturation, $\Delta^{44/40}Ca$ is completely independent of growth rate changes driven by Mn^{2+} and Mg^{2+} inhibition. Calcium isotope fractionation may thus be a useful tool for interpreting calcite supersaturation state, independent of growth rate, in natural systems.

An important caveat is that most natural fluids are significantly more complicated than the solution chemistries investigated here. $\Delta^{44/40}Ca_{calcite\text{-}fluid}$ is predicted to be independent of growth rate inhibition only if the inhibition is driven by a mechanism where kink blocking substantially exceeds the effect of increased solid solution solubility (thus increasing the Ca detachment flux). For some trace elements such as Sr^{2+}, incorporation inhibition is expected be dominant, so the influence of Sr^{2+} on the $\Delta^{44/40}Ca_{calcite\text{-}fluid}$ would be illustrative. Furthermore, unpacking how interactions between inhibitor ions (e.g. Mg^{2+} and SO_4^{2-} (Nielsen et al., 2016)) influence calcite growth mechanics also remains an open area of investigation. This includes potential interactions with 'background electrolyte' ions (Ruiz-Agudo et al., 2010; Ruiz-Agudo et al., 2011), including KCl (used here) and the NaCl that dominates many natural calcite precipitating environments. Fortunately, the results of this work highlight that calcium isotope fractionation, and more broadly stable isotope fractionation, can be used to interrogate the mechanism by which these inhibitors act to inhibit growth - both alone and as part of more complex solution chemistries.

The invariant $\Delta^{44/40}Ca$ with increasing Mg^{2+} leads to two further inferences. First, the difference in $\Delta^{44/40}Ca$ between different calcite faces is likely to be small. Increasing fluid and solid Mg led to substantial morphological changes and progressive expression of non-(1 0 4) calcite faces (Fig. 3) but did not yield measurably different $\Delta^{44/40}Ca$. This is in contrast to the face-specific $\Delta^{44/40}Ca$ in gypsum proposed by Harouaka et al. (2014). Second, the consistent $\Delta^{44/40}Ca$ observed here for experiment Mg7 despite significant precipitation of aragonite may suggest that the $\Delta^{44/40}Ca_{calcite\text{-}fluid}$ and $\Delta^{44/40}Ca_{aragonite\text{-}fluid}$ are more similar during inorganic precipitation than previously believed. Additional data from well-controlled experiments where calcite and aragonite are grown under identical solution conditions is required to further elucidate the differences or lack thereof between calcium isotope fractionation into calcite and aragonite.

4.6. Expanding the microkinetic framework: non-monomer incorporation and beyond

The Mn^{2+} and Mg^{2+} partitioning and inhibition patterns observed here point towards non-monomer incorporation of impurity ions during what appears to be otherwise largely classical calcite growth. This implies that

kinetic models need to explicitly include species other than monomer growth units interacting with and ultimately being incorporated into the mineral lattice, but the identities of these growth units and how they vary with solution composition remains almost completely unknown. Our results suggest that for both Mn^{2+} and Mg^{2+}, cations more strongly hydrated than Ca^{2+}, the species being incorporated at kink sites may be an ion pair, a variably hydrated aquo-complex, or even a larger polynuclear cluster. In the context of the ion-by-ion framework, this will most obviously influence the calculation of kink site probabilities but could also have important implications for kink nucleation dynamics as well as the magnitude of stable isotope fractionation given our current understanding of cation-desolvation driven mass discrimination (Lammers et al., 2020).

Our observations regarding the importance of understanding y_0 sensitivity to inhibitor concentration as well as the apparent changes in growth mechanism with increasing solution and solid Mn^{2+} also highlight the need to better constrain feedbacks between solution chemistry, interfacial energy, local lattice strain, and surface microstructure. While it is more straightforward to predict step velocities, scaling step velocities to bulk growth behavior hinges upon assumptions regarding growth mechanism (i.e. simple spiral or 2D nucleation driven growth (Teng et al., 2000)) and step density. Both y_0 and 2D nucleation rate are sensitive to the fluid-mineral interfacial energy. Better parameterizing links between solution chemistry and interfacial energy is thus a key component of linking micro-scale processes at the fluid-mineral interface to bulk behavior and should be a significant focus of future work.

Finally, while we have demonstrated the utility of calcium stable isotope partitioning as a tracer of crystal growth processes, much more could be learned from the fractionation behavior of trace constituents. The potential utility of using Mg^{2+} isotopes to differentiate between inhibition mechanisms was alluded to here, but there are numerous other cations and anions whose both inhibition and isotope fractionation behavior are of geochemical interest, including Ni^{2+} (Alvarez et al., 2021), Ba^{2+} (Mavromatis et al., 2020), Sr^{2+} (Böhm et al., 2012; AlKhatib and Eisenhauer, 2017b), Zn^{2+} (Mavromatis et al., 2019), and SO_4^{2-} (Barkan et al., 2020). Developing a comprehensive kinetic framework to describe the fractionation of both stoichiometric and trace constituents would both provide a stronger theoretical foundation for interpreting the solution chemistry dependence of those calcite-based proxies and provide important additional constraints on crystal growth dynamics. Explicitly modeling multiple isotope systems at once would provide additional windows into the surficial dynamics in complex solutions and help unravel interactions between inhibitor species. As described above, this will be complicated by the apparent need to account for varying degrees of complexed species interaction with the growing calcite surface, but additional experimental constraints including coupled bulk-growth and in-situ AFM studies in addition to FTIR quantification of water incorporation and lattice-resolved imaging with HRTEM could by help circumvent these complications.

5. CONCLUSIONS

The experimental observations reported here shed light on fundamental aspects of calcite growth in complex solutions. Invariant calcium isotope fractionation during both manganese and magnesium inhibition of calcite growth is indicative of dominantly kink-blocking inhibition behavior. For both cations, which are notably more strongly hydrated than Ca^{2+}, trends in inhibition, partitioning, and isotope fractionation are best explained by non-monomer incorporation of the trace constituent.

The strong growth rate inhibition coupled to large positive K_{Mn} observed at low $\{Mn^{2+}\}/\{Ca^{2+}\}$ cannot be explained by desolvation rate-limited attachment of Mn^{2+}. Instead, our findings suggest Mn^{2+} attaches to kink sites significantly faster than Ca^{2+}, a pattern inconsistent with the slower desolvation kinetics of the Mn^{2+}-aquo complex. We thus posit that the dominant Mn^{2+} species interacting with kink sites is not the free ion in solution but instead an ion pair, hydrated species, or possibly a larger polynuclear cluster. Growth kinetics are then limited by a carbonate-based kink blocking mechanism, driven by slow re-orientation kinetics of carbonate ions that have formed an inner-sphere complex with Mn^{2+} at the surface but must reorient to incorporate into the lattice and/or slow surface desolvation of Mn-occupied kink sites.

For Mg^{2+}, we find that experimental trends are broadly consistent with growth inhibition driven by slow Mg^{2+}-aquo complex dehydration relative to Ca^{2+}. However, that mechanistic explanation likely represents one endmember scenario, seen in Mg-calcite growth at low supersaturations and net precipitation rates. During growth at faster net precipitation rates, our findings are consistent with the incorporation of partially hydrated or otherwise complexed Mg^{2+}, as proposed by Mavromatis et al. (2013) and Alvarez et al. (2021) to explain the rate dependence of Mg^{2+} and Ni^{2+} isotope fractionation during calcite growth. Under these solution conditions, Mg^{2+} desolvation during attachment at kink sites may not be kinetically limiting due to the incorporation of Mg^{2+} complexes, but calcite growth would remain significantly inhibited by the slow kinetics of CO_3^{2-} attachment at Mg^{2+} kink sites.

Taken together, these findings are evocative of a larger trend: that trace constituent cations with aquo-complex desolvation rates significantly slower than the mineral growth rate will tend to be incorporated as a non-monomer species. Additional systematic studies of divalent cation partitioning, inhibition, and stable isotope fractionation behavior of inhibitor cations spanning a range of hydration strengths (e.g. Ni^{2+} to Ba^{2+}) for both calcite and other mineral systems (e.g. sulfates and phosphates) will help test and refine this hypothesis. If supported by findings in other mineral systems, this behavior would have major implications not only for our understanding of the isotopic fractionation of trace species but also fundamental aspects of crystal growth, from defect formation to the controls on the transition from classical to non-classical growth pathways.

DECLARATION OF COMPETING INTEREST

The authors declare that they have no known competing financial interests or personal relationships that could have appeared to influence the work reported in this paper.

ACKNOWLEDGEMENTS

This work was supported by a Berkeley Fellowship to J.V.M, and funding from the DOE Office of Science, Basic Energy Sciences, Division of Chemical, Biological and Geological Sciences under contract no. DE-AC02-05CH11231. The authors wish to thank Rolf Arvidson and two anonymous reviewers whose thoughtful comments improved this manuscript.

APPENDIX A. SUPPLEMENTARY MATERIAL

Supplementary material to this article can be found online at https://doi.org/10.1016/j.gca.2022.06.015.

REFERENCES

Achal V., Pan X. and Zhang D. (2012) Bioremediation of strontium (Sr) contaminated aquifer quartz sand based on carbonate precipitation induced by Sr resistant Halomonas sp. *Chemosphere* **89**, 764–768.

Ahm A.-S.-C., Bjerrum C. J., Blättler C. L., Swart P. K. and Higgins J. A. (2018) Quantifying early marine diagenesis in shallow-water carbonate sediments. *Geochim. Cosmochim. Acta* **236**, 140–159.

AlKhatib M. and Eisenhauer A. (2017a) Calcium and strontium isotope fractionation during precipitation from aqueous solutions as a function of temperature and reaction rate; II. Aragonite. *Geochim. Cosmochim. Acta* **209**, 320–342.

AlKhatib M. and Eisenhauer A. (2017b) Calcium and strontium isotope fractionation in aqueous solutions as a function of temperature and reaction rate; I. Calcite. *Geochim. Cosmochim. Acta* **209**, 296–319.

von Allmen K., Böttcher M. E., Samankassou E. and Nägler T. F. (2010) Barium isotope fractionation in the global barium cycle: First evidence from barium minerals and precipitation experiments. *Chem. Geol.* **277**, 70–77.

Alvarez C. C., Quitté G., Schott J. and Oelkers E. H. (2021) Nickel isotope fractionation as a function of carbonate growth rate during Ni coprecipitation with calcite. *Geochim. Cosmochim. Acta* **299**, 184–198.

Anbeek C. (1993) The effect of natural weathering on dissolution rates. *Geochim. Cosmochim. Acta* **57**, 4963–4975.

Astilleros J. M., Fernández-Díaz L. and Putnis A. (2010) The role of magnesium in the growth of calcite: An AFM study. *Chem. Geol.* **271**, 52–58.

Astilleros J. M., Pina C. M., Fernndez-daz L. and Putnis A. (2002) Molecular-scale surface processes during the growth of calcite in the presence of manganese. *Geochim. Cosmochim. Acta* **66**, 3177–3189.

Barkan Y., Paris G., Webb S. M., Adkins J. F. and Halevy I. (2020) Sulfur isotope fractionation between aqueous and carbonate-associated sulfate in abiotic calcite and aragonite. *Geochim. Cosmochim. Acta* **280**, 317–339.

Barnaby R. J. and Rimstidt D. J. (1989) Redox conditions of calcite cementation interpreted from Mn and Fe contents of authigenic calcites. *GSA Bull.* **101**, 795–804.

Beerling D. J., Kantzas E. P., Lomas M. R., Wade P., Eufrasio R. M., Renforth P., Sarkar B., Andrews M. G., James R. H., Pearce C. R., Mercure J.-F., Pollitt H., Holden P. B., Edwards N. R., Khanna M., Koh L., Quegan S., Pidgeon N. F., Janssens I. A., Hansen J. and Banwart S. A. (2020) Potential for large-scale CO_2 removal via enhanced rock weathering with croplands. *Nature* **583**, 242–248.

Bénézeth P., Saldi G. D., Dandurand J.-L. and Schott J. (2011) Experimental determination of the solubility product of magnesite at 50 to 200°C. *Chem. Geol.* **286**, 21–31.

Berner R. A. (1975) The role of magnesium in the crystal growth of calcite and aragonite from sea water. *Geochim. Cosmochim. Acta* **39**, 489–504.

Bischoff W. D., Bishop F. C. and Mackenzie F. T. (1983) Biogenically produced magnesian calcite; inhomogeneities in chemical and physical properties; comparison with synthetic phases. *Am. Mineral.* **68**, 1183–1188.

Blättler C. L., Henderson G. M. and Jenkyns H. C. (2012) Explaining the Phanerozoic Ca isotope history of seawater. *Geology* **40**, 843–846.

Böhm F., Eisenhauer A., Tang J., Dietzel M., Krabbenhöft A., Kisakürek B. and Horn C. (2012) Strontium isotope fractionation of planktic foraminifera and inorganic calcite. *Geochim. Cosmochim. Acta* **93**, 300–314.

Bourg I. C., Beckingham L. E. and DePaolo D. J. (2015) The Nanoscale Basis of CO_2 Trapping for Geologic Storage. *Environ. Sci. Technol.* **49**, 10265–10284.

Brand U. and Veizer J. (1980) Chemical diagenesis of a multicomponent carbonate system; 1, Trace elements. *J. Sediment. Res.* **50**, 1219–1236.

Burton B. P. and Van de Walle A. (2003) First-principles-based calculations of the $CaCO_3$-$MgCO_3$ and $CdCO_3$-$MgCO_3$ subsolidus phase diagrams. *Phys. Chem. Miner.* **30**, 88–97.

Cabrera N. and Vermilyea D. A. (1958) The growth of crystals from solution. In *Growth and Perfection of Crystals: Proceedings of an International Conference on Crystal Growth* (eds. R. H. Doremus, B. W. Roberts and D. Turnbull). Wiley, New York, NY, pp. 299–358.

Capobianco C. and Navrotsky A. (1987) Solid-solution thermodynamics in $CaCO_3$-$MnCO_3$. *Am. Mineral.* **72**, 312–318.

Chen X.-Y., Teng F.-Z., Sanchez W. R., Romanek C. S., Sanchez-Navas A. and Sánchez-Román M. (2020) Experimental constraints on magnesium isotope fractionation during abiogenic calcite precipitation at room temperature. *Geochim. Cosmochim. Acta* **281**, 102–117.

Chou L., Garrels R. M. and Wollast R. (1989) Comparative study of the kinetics and mechanisms of dissolution of carbonate minerals. *Chem. Geol.* **78**, 269–282.

Clark D. E., Oelkers E. H., Gunnarsson I., Sigfússon B., Snæbjörnsdóttir S. Ó., Aradóttir E. S. and Gíslason S. R. (2020) CarbFix2: CO_2 and H_2S mineralization during 3.5 years of continuous injection into basaltic rocks at more than 250 °C. *Geochim. Cosmochim. Acta* **279**, 45–66.

Davis K. J., Dove P. M., Wasylenki L. E. and De Yoreo J. J. (2004) Morphological consequences of differential Mg^{2+} incorporation at structurally distinct steps on calcite. *Am. Mineral.* **89**, 714.

Davis K. J., Dove P. M. and De Y. J. J. (2000a) Resolving the Control of Magnesium on Calcite Growth: Thermodynamic and Kinetic Consequences of Impurity Incorporation for Biomineral Formation. *MRS Proc.* **620**, M9.5.1.

Davis K. J., Dove P. M. and De Yoreo J. J. (2000b) The Role of Mg^{2+} as an Impurity in Calcite Growth. *Science* **290**, 1134–1137.

DePaolo D. J. (2011) Surface kinetic model for isotopic and trace element fractionation during precipitation of calcite from aqueous solutions. *Geochim. Cosmochim. Acta* **75**, 1039–1056.

Dobberschütz S., Nielsen M. R., Sand K. K., Civioc R., Bovet N., Stipp S. L. S. and Andersson M. P. (2018) The mechanisms of crystal growth inhibition by organic and inorganic inhibitors. *Nat. Commun.* **9**, 1578.

Dove P. M. and Hochella M. F. (1993) Calcite precipitation mechanisms and inhibition by orthophosphate: In situ observations by Scanning Force Microscopy. *Geochim. Cosmochim. Acta* **57**, 705–714.

Dromgoole E. L. and Walter L. M. (1990a) Inhibition of calcite growth rates by Mn^{2+} in $CaCl_2$ solutions at 10, 25, and 50°C. *Geochim. Cosmochim. Acta* **54**, 2991–3000.

Dromgoole E. L. and Walter L. M. (1990b) Iron and manganese incorporation into calcite: Effects of growth kinetics, temperature and solution chemistry. *Chem. Geol.* **81**, 311–336.

Elhadj S., Salter E. A., Wierzbicki A., De Yoreo J. J., Han N. and Dove P. (2006) Peptide Controls on Calcite Mineralization: Polyaspartate Chain Length Affects Growth Kinetics and Acts as a Stereochemical Switch on Morphology. *Cryst. Growth & Des.* **6**, 197–201.

Fairchild I. J. and Baker A. (2012) *Speleothem Science: From Process to Past Environments*. Wiley-Blackwell, Oxford.

Fantle M. S. and Tipper E. T. (2014) Calcium isotopes in the global biogeochemical Ca cycle: Implications for development of a Ca isotope proxy. *Earth-Science Rev.* **129**, 148–177.

Folk R. L. (1974) The natural history of crystalline calcium carbonate; effect of magnesium content and salinity. *J. Sediment. Res.* **44**, 40–53.

Gabitov R. I., Sadekov A. and Leinweber A. (2014) Crystal growth rate effect on Mg/Ca and Sr/Ca partitioning between calcite and fluid: An in situ approach. *Chem. Geol.* **367**, 70–82.

Gebauer D., Völkel A. and Cölfen H. (2008) Stable Prenucleation Calcium Carbonate Clusters. *Science.* **322**, 1819–1822.

Gerdemann S. J., O'Connor W. K., Dahlin D. C., Penner L. R. and Rush H. (2007) Ex Situ Aqueous Mineral Carbonation. *Environ. Sci. Technol.* **41**, 2587–2593.

Gussone N., Ahm A.-S. C., Lau K. V. and Bradbury H. J. (2020) Calcium isotopes in deep time: Potential and limitations. *Chem. Geol.* **544**, 119601.

Gussone N., Böhm F., Eisenhauer A., Dietzel M., Heuser A., Teichert B. M. A., Reitner J., Wörheide G. and Dullo W.-C. (2005) Calcium isotope fractionation in calcite and aragonite. *Geochim. Cosmochim. Acta* **69**, 4485–4494.

Gussone N., Eisenhauer A., Heuser A., Dietzel M., Bock B., Böhm F., Spero H. J., Lea D. W., Bijma J. and Nägler T. F. (2003) Model for kinetic effects on calcium isotope fractionation ($\delta^{44}Ca$) in inorganic aragonite and cultured planktonic foraminifera. *Geochim. Cosmochim. Acta* **67**, 1375–1382.

Harouaka K., Eisenhauer A. and Fantle M. S. (2014) Experimental investigation of Ca isotopic fractionation during abiotic gypsum precipitation. *Geochim. Cosmochim. Acta* **129**, 157–176.

Helm L. and Merbach A. E. (1999) Water exchange on metal ions: experiments and simulations. *Coord. Chem. Rev.* **187**, 151–181.

Hem J. D. (1963) *Chemical equilibria and rates of manganese oxidation*. US Government Printing Office.

Higgins J. A., Blättler C. L., Lundstrom E. A., Santiago-Ramos D. P., Akhtar A. A., Ahm A.-S.-C., Bialik O., Holmden C., Bradbury H., Murray S. T. and Swart P. K. (2018) Mineralogy, early marine diagenesis, and the chemistry of shallow-water carbonate sediments. *Geochim. Cosmochim. Acta* **220**, 512–534.

Higgins S. R. and Hu X. (2005) Self-limiting growth on dolomite: Experimental observations with in situ atomic force microscopy. *Geochim. Cosmochim. Acta* **69**, 2085–2094.

Hong M. and Teng H. H. (2014) Implications of solution chemistry effects: Direction-specific restraints on the step kinetics of calcite growth. *Geochim. Cosmochim. Acta* **141**, 228–239.

Hong M., Xu J. and Teng H. H. (2016) Evolution of calcite growth morphology in the presence of magnesium: Implications for the dolomite problem. *Geochim. Cosmochim. Acta* **172**, 55–64.

Immenhauser A., Buhl D., Richter D., Niedermayr A., Riechelmann D., Dietzel M. and Schulte U. (2010) Magnesium-isotope fractionation during low-Mg calcite precipitation in a limestone cave – Field study and experiments. *Geochim. Cosmochim. Acta* **74**, 4346–4364.

Jiménez-López C., Romanek C. S., Huertas F. J., Ohmoto H. and Caballero E. (2004) Oxygen isotope fractionation in synthetic magnesian calcite. *Geochim. Cosmochim. Acta* **68**, 3367–3377.

Johnson K. S. (1982) Solubility of rhodochrosite ($MnCO_3$) in water and seawater. *Geochim. Cosmochim. Acta* **46**, 1805–1809.

Katsikopoulos D., Fernández-González Á. and Prieto M. (2009) Precipitation and mixing properties of the "disordered" (Mn, Ca)CO_3 solid solution. *Geochim. Cosmochim. Acta* **73**, 6147–6161.

Kelemen P. B., Matter J., Streit E. E., Rudge J. F., Curry W. B. and Blusztajn J. (2011) Rates and Mechanisms of Mineral Carbonation in Peridotite: Natural Processes and Recipes for Enhanced, in situ CO_2 Capture and Storage. *Annu. Rev. Earth Planet. Sci.* **39**, 545–576.

Kelemen P. B., McQueen N., Wilcox J., Renforth P., Dipple G. and Vankeuren A. P. (2020) Engineered carbon mineralization in ultramafic rocks for CO_2 removal from air: Review and new insights. *Chem. Geol.* **550** 119628.

Kump L. R., Brantley S. L. and Arthur M. A. (2000) Chemical Weathering, Atmospheric CO_2, and Climate. *Annu. Rev. Earth Planet. Sci.* **28**, 611–667.

De La Pierre M., Raiteri P. and Gale J. D. (2016) Structure and Dynamics of Water at Step Edges on the Calcite 1014 Surface. *Cryst. Growth Des.* **16**, 5907–5914.

Lammers L. N., Kulasinski K., Zarzycki P. and DePaolo D. J. (2020) Molecular simulations of kinetic stable calcium isotope fractionation at the calcite-aqueous interface. *Chem. Geol.* **532** 119315.

Lammers L. N. and Mitnick E. H. (2019) Magnesian calcite solid solution thermodynamics inferred from authigenic deep-sea carbonate. *Geochim. Cosmochim. Acta* **248**, 343–355.

Langmuir D. (1979) Techniques of Estimating Thermodynamic Properties for Some Aqueous Complexes of Geochemical Interest. *Chem. Model. Aqueous Syst.* **93**, 18–353.

Lardge J. S., Duffy D. M., Gillan M. J. and Watkins M. (2010) Ab Initio Simulations of the Interaction between Water and Defects on the Calcite (1014) Surface. *J. Phys. Chem. C* **114**, 2664–2668.

Lin Y.-P. and Singer P. C. (2009) Effect of Mg^{2+} on the kinetics of calcite crystal growth. *J. Cryst. Growth* **312**, 136–140.

Lorens R. B. (1981) Sr, Cd, Mn and Co distribution coefficients in calcite as a function of calcite precipitation rate. *Geochim. Cosmochim. Acta* **45**, 553–561.

Lukashev V. K. (1993) Some geochemical and environmental aspects of the Chernobyl nuclear accident. *Appl. Geochem.* **8**, 419–436.

Luo Y. and Millero F. J. (2003) Solubility of Rhodochrosite ($MnCO_3$) in NaCl Solutions. *J. Solution Chem.* **32**, 405–416.

Maher K., Johnson N. C., Jackson A., Lammers L. N., Torchinsky A. B., Weaver K. L., Bird D. K. and Brown G. E. (2016) A spatially resolved surface kinetic model for forsterite dissolution. *Geochim. Cosmochim. Acta* **174**, 313–334.

Maher K., Steefel C. I., DePaolo D. J. and Viani B. E. (2006) The mineral dissolution rate conundrum: Insights from reactive transport modeling of U isotopes and pore fluid chemistry in marine sediments. *Geochim. Cosmochim. Acta* **70**, 337–363.

Mavromatis V., Gautier Q., Bosc O. and Schott J. (2013) Kinetics of Mg partition and Mg stable isotope fractionation during its

incorporation in calcite. *Geochim. Cosmochim. Acta* **114**, 188–203.

Mavromatis V., González A. G., Dietzel M. and Schott J. (2019) Zinc isotope fractionation during the inorganic precipitation of calcite - Towards a new pH proxy. *Geochim. Cosmochim. Acta* **244**, 99–112.

Mavromatis V., van Zuilen K., Blanchard M., van Zuilen M., Dietzel M. and Schott J. (2020) Experimental and theoretical modelling of kinetic and equilibrium Ba isotope fractionation during calcite and aragonite precipitation. *Geochim. Cosmochim. Acta* **269**, 566–580.

McQueen N., Kelemen P., Dipple G., Renforth P. and Wilcox J. (2020) Ambient weathering of magnesium oxide for CO_2 removal from air. *Nat. Commun.* **11**, 3299.

Mills J. V., DePaolo D. J. and Lammers L. N. (2021) The influence of Ca:CO_3 stoichiometry on Ca isotope fractionation: Implications for process-based models of calcite growth. *Geochim. Cosmochim. Acta* **298**, 87–111.

Mittemeijer E. J. and Welzel U. (2008) The "state of the art" of the diffraction analysis of crystallite size and lattice strain. *Zeitschrift für Krist.* **223**, 552–560.

Morgan J. (1967) Chemical equilibria and kinetic properties of manganese in natural water. In *Principles and applications of water chemistry*. Wiley, pp. 561–623.

Morgan J. J. (2005) Kinetics of reaction between O_2 and Mn(II) species in aqueous solutions. *Geochim. Cosmochim. Acta* **69**, 35–48.

Morse J. W., Arvidson R. S. and Lüttge A. (2007) Calcium Carbonate Formation and Dissolution. *Chem. Rev.* **107**, 342–381.

Mucci A. (1987) Influence of temperature on the composition of magnesian calcite overgrowths precipitated from seawater. *Geochim. Cosmochim. Acta* **51**, 1977–1984.

Mucci A. (1988) Manganese uptake during calcite precipitation from seawater: Conditions leading to the formation of a pseudokutnahorite. *Geochim. Cosmochim. Acta* **52**, 1859–1868.

Mucci A. and Morse J. W. (1983) The incorporation of Mg^{2+} and Sr^{2+} into calcite overgrowths: influences of growth rate and solution composition. *Geochim. Cosmochim. Acta* **47**, 217–233.

Navrotsky A. and Capobianco C. (1987) Enthalpies of formation of dolomite and of magnesian calcites. *Am. Mineral.* **72**, 782–787.

Nielsen L. C., DePaolo D. J. and De Yoreo J. J. (2012) Self-consistent ion-by-ion growth model for kinetic isotopic fractionation during calcite precipitation. *Geochim. Cosmochim. Acta* **86**, 166–181.

Nielsen L. C., De Yoreo J. J. and DePaolo D. J. (2013) General model for calcite growth kinetics in the presence of impurity ions. *Geochim. Cosmochim. Acta* **115**, 100–114.

Nielsen M. R., Sand K. K., Rodriguez-Blanco J. D., Bovet N., Generosi J., Dalby K. N. and Stipp S. L. S. (2016) Inhibition of Calcite Growth: Combined Effects of Mg^{2+} and SO_4^{2-}. *Cryst. Growth Des.* **16**, 6199–6207.

Paquette J. and Reeder R. J. (1990) New type of compositional zoning in calcite: Insights into crystal-growth mechanisms. *Geology* **18**, 1244–1247.

Paquette J. and Reeder R. J. (1995) Relationship between surface structure, growth mechanism, and trace element incorporation in calcite. *Geochim. Cosmochim. Acta* **59**, 735–749.

Parkhurst D. L. and Appelo C. A. J. (2013) Description of input and examples for PHREEQC version 3 - A computer program for speciation, batch-reaction, one-dimensional transport, and inverse geochemical calculations. In *U.S. Geological Survey Techniques and Methods, book 6, chap. A43*, p. 497.

Pimentel C., Pina C. M. and Gnecco E. (2013) Epitaxial Growth of Calcite Crystals on Dolomite and Kutnahorite (104) Surfaces. *Cryst. Growth Des.* **13**, 2557–2563.

Pingitore N. E., Eastman M. P., Sandidge M., Oden K. and Freiha B. (1988) The coprecipitation of manganese(II) with calcite: an experimental study. *Mar. Chem.* **25**, 107–120.

Plummer L. N. and Busenberg E. (1982) The solubilities of calcite, aragonite and vaterite in CO_2-H_2O solutions between 0 and 90° C, and an evaluation of the aqueous model for the system $CaCO_3$-CO_2-H_2O. *Geochim. Cosmochim. Acta* **46**, 1011–1040.

Pokrovsky O. S., Golubev S. V., Schott J. and Castillo A. (2009) Calcite, dolomite and magnesite dissolution kinetics in aqueous solutions at acid to circumneutral pH, 25 to 150°C and 1 to 55 atm pCO_2: New constraints on CO_2 sequestration in sedimentary basins. *Chem. Geol.* **265**, 20–32.

Prieto M., Astilleros J. M. and Fernández-Díaz L. (2013) Environmental Remediation by Crystallization of Solid Solutions. *Elements* **9**, 195–201.

Ravizza G. E. and Zachos J. C. (2003) Records of Cenozoic ocean chemistry ed. H. Elderfield. *Treatise Geochem.* **6**, 551–581.

Reardon E. J. and Langmuir D. (1974) Thermodynamic properties of the ion pairs $MgCO_3^0$ and $CaCO_3^0$ from 10 to 50 degrees C. *Am. J. Sci.* **274**, 599–612.

Reddy M. M. and Wang K. K. (1980) Crystallization of calcium carbonate in the presence of metal ions: I. Inhibition by magnesium ion at pH 8.8 and 25°C. *J. Cryst. Growth* **50**, 470–480.

Reeder R. J. (1996) Interaction of divalent cobalt, zinc, cadmium, and barium with the calcite surface during layer growth. *Geochim. Cosmochim. Acta* **60**, 1543–1552.

Reeder R. J. and Grams J. C. (1987) Sector zoning in calcite cement crystals: Implications for trace element distributions in carbonates. *Geochim. Cosmochim. Acta* **51**, 187–194.

Reischl B., Raiteri P., Gale J. D. and Rohl A. L. (2019) Atomistic Simulation of Atomic Force Microscopy Imaging of Hydration Layers on Calcite, Dolomite, and Magnesite Surfaces. *J. Phys. Chem. C* **123**, 14985–14992.

Renforth P., Manning D. A. C. and Lopez-Capel E. (2009) Carbonate precipitation in artificial soils as a sink for atmospheric carbon dioxide. *Appl. Geochem.* **24**, 1757–1764.

Robie R. A., Haselton, Jr., H. T. and Hemingway B. S. (1984) Heat capacities and entropies of rhodochrosite ($MnCO_3$) and siderite ($FeCO_3$) between 5 and 600 K. *Am. Mineral.* **69**, 349–357.

Rodriguez-Navarro C., Kudlacz K., Cizer O. and Ruiz-Agudo E. (2015) Formation of amorphous calcium carbonate and its transformation into mesostructured calcite. *CrystEngComm* **17**, 58–72.

Ruiz-Agudo E., Kowacz M., Putnis C. V. and Putnis A. (2010) The role of background electrolytes on the kinetics and mechanism of calcite dissolution. *Geochim. Cosmochim. Acta* **74**, 1256–1267.

Ruiz-Agudo E., Putnis C. V., Wang L. and Putnis A. (2011) Specific effects of background electrolytes on the kinetics of step propagation during calcite growth. *Geochim. Cosmochim. Acta* **75**, 3803–3814.

Schott J., Mavromatis V., Fujii T., Pearce C. R. and Oelkers E. H. (2016) The control of carbonate mineral Mg isotope composition by aqueous speciation: Theoretical and experimental modeling. *Chem. Geol.* **445**, 120–134.

Sethmann I., Wang J., Becker U. and Putnis A. (2010) Strain-Induced Segmentation of Magnesian Calcite Thin Films Growing on a Calcite Substrate. *Cryst. Growth Des.* **10**, 4319–4326.

Shannon R. D. (1976) Revised effective ionic radii and systematic studies of interatomic distances in halides and chalcogenides. *Acta Crystallogr. Sect. A* **32**, 751–767.

Stack A. G. and Grantham M. C. (2010) Growth Rate of Calcite Steps As a Function of Aqueous Calcium-to-Carbonate Ratio:

Independent Attachment and Detachment of Calcium and Carbonate Ions. *Cryst. Growth Des.* **10**, 1409–1413.

Staudt W. J., Reeder R. J. and Schoonen M. A. A. (1994) Surface structural controls on compositional zoning of SO_2^4 and SeO_2^4 in synthetic calcite single crystals. *Geochim. Cosmochim. Acta* **58**, 2087–2098.

Stephenson A. E., Hunter J. L., Han N., DeYoreo J. J. and Dove P. M. (2011) Effect of ionic strength on the Mg content of calcite: Toward a physical basis for minor element uptake during step growth. *Geochim. Cosmochim. Acta* **75**, 4340–4350.

Sternbeck J. (1997) Kinetics of rhodochrosite crystal growth at 25° C: The role of surface speciation. *Geochim. Cosmochim. Acta* **61**, 785–793.

Tang J., Dietzel M., Bohm F., Kohler S. J. and Eisenhauer A. (2008) Sr^{2+}/Ca^{2+} and $^{44}Ca/^{40}Ca$ fractionation during inorganic calcite formation: II. Ca isotopes. *Geochim. Cosmochim. Acta* **72**, 3733–3745.

Temmam M., Paquette J. and Vali H. (2000) Mn and Zn incorporation into calcite as a function of chloride aqueous concentration. *Geochim. Cosmochim. Acta* **64**, 2417–2430.

Teng H. H., Dove P. M. and De Yoreo J. J. (2000) Kinetics of calcite growth: surface processes and relationships to macroscopic rate laws. *Geochim. Cosmochim. Acta* **64**, 2255–2266.

Turner D. R., Whitfield M. and Dickson A. G. (1981) The equilibrium speciation of dissolved components in freshwater and sea water at 25°C and 1 atm pressure. *Geochim. Cosmochim. Acta* **45**, 855–881.

Vinson M. D., Arvidson R. S. and Luttge A. (2007) Kinetic inhibition of calcite (104) dissolution by aqueous manganese (II). *J. Cryst. Growth* **307**, 116–125.

Wang Q., Grau-Crespo R. and de Leeuw N. H. (2011) Mixing Thermodynamics of the Calcite-Structured (Mn, Ca)CO_3 Solid Solution: A Computer Simulation Study. *J. Phys. Chem. B* **115**, 13854–13861.

Wasylenki L. E., Dove P. M., Wilson D. S. and De Yoreo J. J. (2005a) Nanoscale effects of strontium on calcite growth: An in situ AFM study in the absence of vital effects. *Geochim. Cosmochim. Acta* **69**, 3017–3027.

Wasylenki L. E., Dove P. M. and De Y. J. J. (2005b) Effects of temperature and transport conditions on calcite growth in the presence of Mg^{2+}: Implications for paleothermometry. *Geochim. Cosmochim. Acta* **69**, 4227–4236.

Watkins J. M., Nielsen L. C., Ryerson F. J. and DePaolo D. J. (2013) The influence of kinetics on the oxygen isotope composition of calcium carbonate. *Earth Planet. Sci. Lett.* **375**, 349–360.

Wolfram O. and Krupp R. E. (1996) Hydrothermal solubility of rhodochrosite, Mn (II) speciation, and equilibrium constants. *Geochim. Cosmochim. Acta* **60**, 3983–3994.

Wolthers M., Nehrke G., Gustafsson J. P. and Van Cappellen P. (2012) Calcite growth kinetics: Modeling the effect of solution stoichiometry. *Geochim. Cosmochim. Acta* **77**, 121–134.

Wolthers M., Tommaso D., Di D. Z. and de Leeuw N. H. (2013) Variations in calcite growth kinetics with surface topography: molecular dynamics simulations and process-based growth kinetics modelling. *CrystEngComm* **15**, 5506–5514.

De Yoreo J. J. and Vekilov P. G. (2003) Principles of Crystal Nucleation and Growth. *Rev. Mineral. Geochem.* **54**, 57–93.

Zhang Y. and Dawe R. A. (2000) Influence of Mg^{2+} on the kinetics of calcite precipitation and calcite crystal morphology. *Chem. Geol.* **163**, 129–138.

Zhu G., Yao S., Zhai H., Liu Z., Li Y., Pan H. and Tang R. (2016) Evolution from Classical to Non-classical Aggregation-Based Crystal Growth of Calcite by Organic Additive Control. *Langmuir* **32**, 8999–9004.

Associate editor: Oleg Pokrovsky